Hemoglobin nanoclusters-mediated regulation of KPNA4 in hypoxic tumor microenvironment enhances photodynamic therapy in hepatocellular carcinoma

Yiliang Wang[1†], Nu Li[2†], Letian Qu[3†], Mu Zhang[3], Zhuo Li[4], Xiang Li[5*] and Dasheng Cai[1*]

Abstract

Background Hepatocellular carcinoma (HCC) is a highly malignant tumor known for its hypoxic environment, which contributes to resistance against the anticancer drug Sorafenib (SF). Addressing SF resistance in HCC requires innovative strategies to improve tumor oxygenation and effectively deliver therapeutics.

Results In our study, we explored the role of KPNA4 in mediating hypoxia-induced SF resistance in HCC. We developed hemoglobin nanoclusters (Hb-NCs) capable of carrying oxygen, loaded with indocyanine green (ICG) and SF, named HPRG@SF. In vitro, HPRG@SF targeted HCC cells, alleviated hypoxia, suppressed KPNA4 expression, and enhanced the cytotoxicity of PDT against hypoxic, SF-resistant HCC cells. In vivo experiments supported these findings, showing that HPRG@SF effectively improved the oxygenation within the tumor microenvironment and countered SF resistance through combined photodynamic therapy (PDT).

Conclusion The combination of Hb-NCs with ICG and SF, forming HPRG@SF, presents a potent strategy to overcome drug resistance in hepatocellular carcinoma by improving hypoxia and employing PDT. This approach not only targets the hypoxic conditions that underlie resistance but also provides a synergistic anticancer effect, highlighting its potential for clinical applications in treating resistant HCC.

Keywords Hepatocellular carcinoma, Hypoxia, Sorafenib, Drug resistance, Mitochondrial function, Hemoglobin nanocluster complexes, KPNA4, Photodynamic therapy

---

†Yiliang Wang, Nu Li and Letian Qu regarded as co-first authors.

*Correspondence:
Xiang Li
lixiangxmn11@163.com
Dasheng Cai
cds1225@sina.com
1Department of Anesthesiology, The First Hospital of China Medical University, No. 155, Nanjing North Street, Heping District, Shenyang 110001, Liaoning Province, China

2Department of breast surgery, The First Hospital of China Medical University, Shenyang 110001, Liaoning Province, China
3Department of Geriatrics, The First Hospital of China Medical University, Shenyang 110001, Liaoning Province, China
4The Fourth People's Hospital of Shenyang, 110002 Liaoning Province, China
5Department of Neurosurgery, The First Hospital of China Medical University, No. 155, Nanjing North Street, Heping District, Shenyang 110001, Liaoning Province, China

Wang *et al. Journal of Nanobiotechnology*   (2024) 22:473

Page 2 of 25

Introduction

Hepatocellular carcinoma (HCC) is a highly prevalent tumor that poses significant treatment challenges [1–3]. Chemotherapy and surgical resection are commonly used approaches for HCC treatment; however, they have limitations [4, 5]. The importance of the tumor microenvironment in HCC treatment is well recognized, particularly the formation of a hypoxic environment, which significantly influences treatment outcomes [6–8].

Hypoxia refers to a lack of oxygen within the tumor caused by acidosis, uneven blood vessel distribution, and high metabolic activity [9]. Studies have revealed the pivotal role of hypoxia in HCC drug resistance [10, 11]. Hypoxia triggers intracellular stress responses, including mitochondrial dysfunction and enhanced cellular resistance to drugs [12, 13]. Moreover, hypoxia constrains the efficacy of Sorafenib (SF), a commonly used drug for HCC treatment [14–16]. For example, SF's therapeutic effectiveness is restricted by the hypoxic environment [14, 15, 17].

In recent years, studies have employed techniques such as single-cell RNA sequencing (scRNA-seq) and transcriptome data analysis to identify differentially expressed genes related to hypoxia from the GEO database and further validated their roles in HCC through in vitro experiments [18, 19].

Hemoglobin (Hb) nanoclusters (NCs) possess oxygen-carrying capabilities and hold the potential for improving hypoxic environments and reshaping mitochondrial function in cells [20]. Researchers successfully constructed HPRG@SF nanocomposites by loading organic indocyanine green (ICG) and SF [21–23].

The objective of this study is to reverse HCC resistance to SF by improving the hypoxic environment and combining it with PDT. We aim to provide a better treatment option for hypoxic-type HCC patients using this novel therapeutic strategy. The results of this study will offer new theoretical and practical guidance for the advancement of HCC treatment and regulation of the hypoxic tumor microenvironment, with significant scientific and clinical implications. By resolving the issue of HCC drug resistance caused by hypoxia, we anticipate offering more effective treatment options for HCC patients and promoting further developments in liver cancer research.

Results and discussion

Unveiling the role of hypoxia in drug resistance of HCC cells

SF is a novel multi-targeted drug used for treating HCC [24]. However, studies have shown that the hypoxic environment promotes the survival and proliferation of HCC cells by activating various signaling pathways, and it can also activate stress responses within tumor cells, leading to resistance to SF and acquisition of drug resistance [25].

Therefore, in this study, we aimed to explore the mechanisms of hypoxia-induced HCC drug resistance and provide an effective method to overcome hypoxia and combat SF resistance.

To perform our analysis, we obtained the HCC-related scRNA-seq dataset GSE202642 from the GEO database, which included 7 HCC samples and 4 adjacent normal tissue samples. The analysis workflow is shown in Fig. 1A. Initially, we integrated the data using the Seurat package, filtering out cells with low gene counts (nFeature_RNA < 5000), low mRNA molecule counts (nCount_RNA < 20,000), and high mitochondrial gene percentages (percent.mt < 20%) (Figure S1A). Then, we further filtered the cells based on the criteria of 200 < nFeature_RNA < 5000 and percent.mt < 10% to remove low-quality cells, resulting in an expression matrix of 38,081 genes and 85,147 cells. The correlation analysis of sequencing depth showed $r = -0.05$ between filtered data nCount_RNA and percent.mt, and $r = 0.88$ between nCount_RNA and nFeature_RNA (Figure S1B), indicating that the filtered cell data had good quality and could be used for subsequent analysis.

Next, we analyzed the filtered cells using the CellCycleScoring function to calculate the cell cycle of the samples (Figure S1C) and performed initial normalization of the data. We selected highly variable genes based on gene expression variance and chose the top 2000 genes with the highest variance for downstream analysis (Figure S2A). Subsequently, we performed linear dimension reduction of the data using PCA. Here, we present the heatmap of the major correlated gene expression values for PC_1 - PC_6 (Figure S1D) and the distribution of cells in PC_1 and PC_2 (Figure S1E-F), which showed that there were certain batch effects between samples. To eliminate batch effects and improve the accuracy of cell clustering, we performed batch correction using the harmony package. Additionally, we used ElbowPlot to sort the standard deviations of the PCs and found that PC_1 - PC_20 adequately reflected the information contained in the selected highly variable genes and had good analytical significance (Figure S2B). The results after correction showed that batch effects were effectively removed (Figure S2C-D).

Then, we applied the UMAP algorithm for non-linear dimension reduction of the top 20 principal components and used the cluster package to visualize the clustering at different resolutions (Figure S3A). Based on the clustering results, we selected a resolution of 0.3 and obtained 17 cell clusters (Figure S2E-F). The marker genes for each cell cluster are shown in Figure S2G-H. We annotated the cells using known lineage-specific marker genes obtained from literature research and the online resource CellMarker (Fig. 1B), resulting in the identification of 8 cell types. Based on the marker genes CD7, CD3D, and
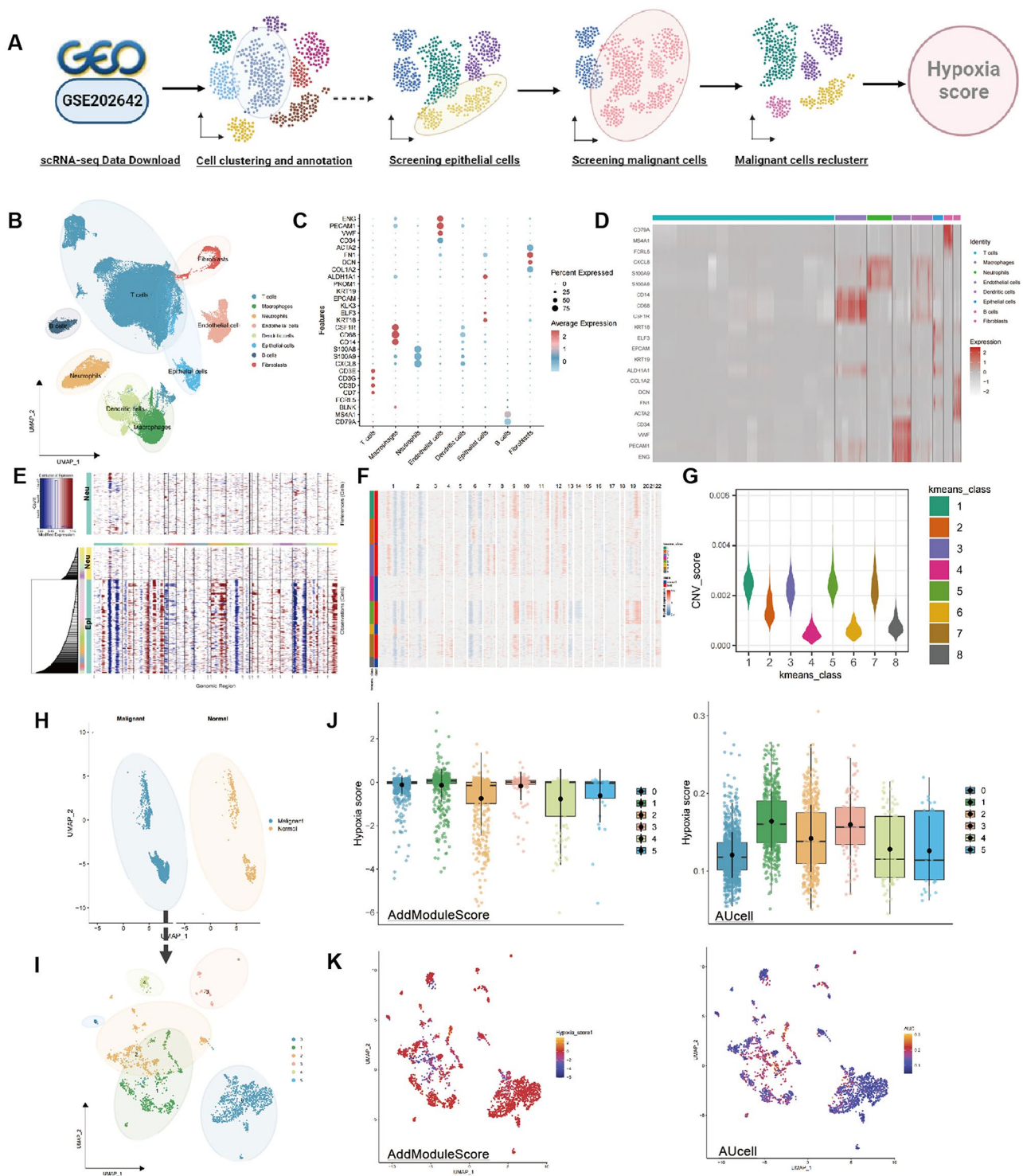
Fig. 1 scRNA-seq cell annotation and hypoxia malignant cell extraction. Note: (**A**) Schematic diagram illustrating the analysis of screening hypoxia malignant cells from scRNA-seq data; (**B**) UMAP clustering distributions of 8 cell types, where each color represents a subpopulation of cells; (**C**) Bubble plot showing expression of marker genes in the 8 cell types, with larger circles indicating higher expression levels and darker red indicating higher average expression levels; (**D**) Heatmap displaying expression of marker genes in the 8 cell types, with darker red indicating higher average expression levels; (**E**) CNV analysis of epithelial cells, where the top section in cyan represents Reference Neutrophil cells, the bottom section in yellow represents included normal Neutrophil cells, and the cyan cells represent extracted epithelial cells, with blue indicating DNA copy loss and red indicating DNA copy gain; (**F**) K-means clustering algorithm applied to the cells in "Observation" from the Figure E; (**G**) CNV scores after K-means clustering; (**H**) UMAP plot of epithelial cells, with cyan representing malignant epithelial cells and black representing normal epithelial cells; (**I**) UMAP plot of re-clustered malignant epithelial cells; (**J**) Hypoxia scores of malignant cell subpopulations; (**K**) UMAP mapping of hypoxia scores from malignant cell subpopulations. HCC samples: 7 cases, normal tissue samples: 4 cases
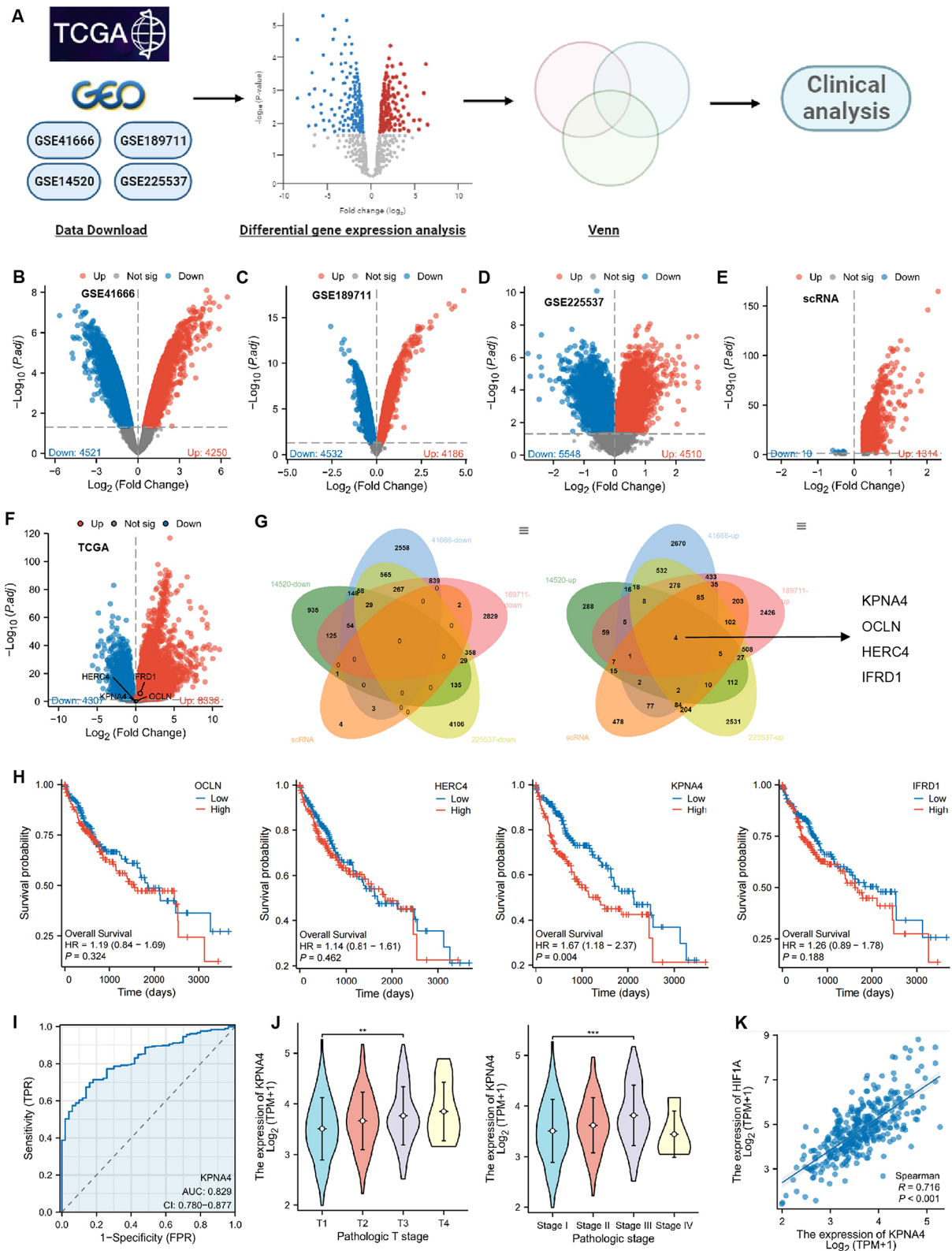
Fig. 2 (See legend on next page.)

(See figure on previous page.)
Fig. 2 The key genes involved in regulating HCC resistance to SF. Note: (**A**) Fig. 2 illustrates the bioinformatics analysis workflow; (**B**) The volcano plot of differentially expressed genes in the GSE41666 dataset, where gray represents genes with no differential expression, red indicates upregulated genes, and green indicates downregulated genes. The normoxic group consisted of 3 samples, and the hypoxic group consisted of 3 samples; (**C**) The volcano plot of differentially expressed genes in the GSE189711 dataset, with 3 samples in the SF-sensitive group and 3 samples in the SF-resistant group; (**D**) The volcano plot of differentially expressed genes in the GSE225537 dataset, with 4 samples in the control group and 4 samples in the SF treatment group; (**E**) Differential expression genes between high-scoring hypoxic malignant cells and other low-hypoxic malignant cells in the scRNA dataset; (**F**) The volcano plot of differentially expressed genes in the TCGA-LIHC dataset; (**G**) Venn diagram showing the intersection of upregulated and downregulated genes across various datasets; (**H**) Survival analysis of various genes in the TCGA-LIHC dataset; (**I**) ROC analysis of KPNA4 in relation to patient outcomes in the TCGA-LIHC dataset; (**J**) Expression changes of KPNA4 in relation to different T stages and stages in the TCGA-LIHC dataset, with 374 cases of adjacent tissues and HCC tissues. * indicates intergroup comparison, **$P < 0.01$, ***$P < 0.001$. (**K**) Correlation analysis of KPNA4 and the hypoxia factor HIF-1α in the TCGA-LIHC dataset

CD3G, we annotated clusters 0, 1, 4, 6, 10, 12, 14, and 15, 16 as T cells. Cluster 11 was annotated as B cells based on the marker genes CD79A and MS4A1. Cluster 3 was considered to be a Neutrophil based on the marker genes CXCL8, S100A9, and S100A8. Cluster 2 was annotated as Macrophages based on the marker genes CD14, CD68, and CSF1R. Cluster 8 was annotated as Epithelial cells based on the marker genes KRT18, ELF3, EPCAM, ALDH1A1, and KRT19. Cluster 13 was annotated as Fibroblasts based on the marker genes COL1A2, DCN, FN1, and ACTA2. Cluster 5 was annotated as Endothelial cells based on the marker genes CD34, VWF, PECAM1, and ENG. Cluster 7 and 9 were annotated as Dendritic cells based on the marker gene ITGAX (Fig. 1C-D). By observing the proportion of cell populations in HCC samples and normal samples, we found that T cells were the most abundant, followed by macrophages and neutrophils, and there were differences in cell composition between different samples (Figure S3B-C).

HCC is the most common pathological type of liver cancer, originating from hepatocyte epithelial tissue. Therefore, we further extracted malignant cells from epithelial cells for analysis. In this step, we used the "inferCNV" package to detect large-scale copy number variations (CNVs) in cells, using neutrophils as a control. The results showed that most of the epithelial cells exhibited CNV (Fig. 1E). Subsequently, we formed 8 clusters of normal cells and epithelial cells based on "Observation" and found that clusters 2, 4, 6, and 8 contained all the normal cells and had lower CNV scores. After excluding these clusters, we obtained 2,357 malignant epithelial cells (Fig. 1F-H). We further grouped the obtained malignant epithelial cells into 6 clusters (Fig. 1I). Then, we used the GSEA database to evaluate the hypoxic scores of these 6 malignant cells by using the AddModuleScore function and AuCell function, as shown in Fig. 1J-K. Cluster 1 and 3 had significantly higher hypoxic scores compared to clusters 0, 2, 4, and 5. Therefore, we identified clusters 1 and 3 as hypoxic malignant HCC cells.

In summary, our results revealed 8 cell subgroups, successfully isolated malignant cells from epithelial cells and extracted high-hypoxia-score cell clusters for further analysis.

Identification of key factors mediating hypoxia-Induced drug resistance in HCC

Next, we integrated scRNA-seq data with bulk RNA-seq data to identify key factors responsible for HCC resistance to SF under hypoxia. A schematic diagram illustrating the process is shown in Fig. 2A. Initially, we downloaded the HCC transcriptome dataset GSE14520 from the GEO database and used WGCNA to identify core genes associated with HCC. Using a correlation threshold of 0.9, we selected a soft thresholding parameter β of 6 (Figure S4A-B). Subsequently, we constructed 17 co-expression modules through WGCNA analysis (Figure S4C). Among them, the module-trait relationship analysis revealed a significant positive correlation between the yellow module and HCC, with 1299 genes showing a strong correlation, while the violet module showed a significant negative correlation with HCC and consisted of 3657 genes (Figure S4D-E). Differential expression analysis of the GSE14520 dataset identified 3324 upregulated genes and 2761 downregulated genes (Figure S4F). By intersecting the WGCNA core genes with the differentially expressed genes, we obtained 579 upregulated genes and 1514 downregulated genes (Figure S4G).

Further, we performed differential expression analysis on the HCC cell datasets GSE41666 and GSE189711 under normoxic and hypoxic conditions, as well as the dataset GSE225537 representing SF-sensitive and SF-resistant HCC cells. This analysis yielded a list of upregulated and downregulated genes specific to each dataset (Fig. 2B-D). Additionally, we conducted differential expression analysis on high-scoring malignant cells and low-scoring malignant cells from the scRNA-seq dataset (Fig. 2E) and also performed differential expression analysis on the LIHC expression profile from TCGA (Fig. 2F). Lastly, by combining all the differentially expressed genes from these datasets and considering the intersection of upregulated and downregulated genes, we identified four upregulated genes: KPNA4, OCLN, HERC4, and IFRD1 (Fig. 2G).

Based on the clinical data from TCGA LIHC, we found that among these four genes, only KPNA4 showed a significant association with survival (Fig. 2H), with an AUC

value of 0.829, indicating good diagnostic performance for outcome prediction (Fig. 2I). Furthermore, KPNA4 expression exhibited significant incremental changes in different T stages and stages (Fig. 2J). In addition, KPNA4 was significantly positively correlated with the hypoxia factor HIF-1α, consistent with our expectations (Fig. 2K). Therefore, based on these findings, KPNA4 may play a crucial role in promoting hypoxia-mediated HCC resistance to SF.

Oxygen deprivation induces KPNA4 activation and mitochondrial stability, leading to SF resistance in HCC cells

To investigate the regulation of KPNA4 on SF resistance under hypoxic conditions, three HCC cell lines (Huh7, MHCC97H, and MHCC97L) were cultured under normoxic or hypoxic conditions. The expression levels of KPNA4 and the hypoxia-inducible factor HIF-1α were measured, and the results showed a significant increase in KPNA4 and HIF-1α expression under hypoxic conditions in all three HCC cell lines (Figure S5A). Additionally, the HCC cells exhibited resistance to SF under hypoxic conditions (Figure S5B-C). Previous research has demonstrated that SF exerts its toxicity on HCC cells by stimulating the production of ROS [26]. Thus, when HCC cells were treated with SF under different oxygen conditions, there was a significant decrease in ROS production under hypoxic conditions compared to normoxic conditions (Figure S5D), indicating that hypoxia promotes SF resistance in HCC cells (Figure S5E). Among the cell lines tested, MHCC97H exhibited the highest resistance, making it the selected cell line for subsequent in vitro experiments.

ROS is closely associated with mitochondrial activity [26]. To determine whether hypoxic conditions affect the production of ROS that downregulate SF via mitochondria, the mitochondrial content in MHCC97H cells was measured, and the results revealed a significant decrease in both mitochondrial numbers and DNA content under hypoxic conditions (Figure S6A-B). Additionally, the OCR of the drug-resistant cells was significantly reduced under hypoxic conditions, indicating a decrease in mitochondrial respiratory capacity (Figure S6C). SF, as a multi-kinase inhibitor, has been shown to regulate the oxidative-reductive state of drug-resistant cancer cells [27]. Therefore, the redox balance between oxidation and reduction was examined under normoxic and hypoxic conditions, revealing a more reduced state under hypoxic conditions compared to normoxic conditions (Figure S6D). Finally, the changes in mitochondria in response to SF treatment under different oxygen conditions were assessed, and it was observed that while MMP decreased significantly in both normoxic and hypoxic conditions, the reduction was more pronounced under normoxic

conditions (Figure S6E). Moreover, TEM results showed that SF treatment led to partial mitochondrial degradation in MHCC97H cells under normoxic conditions, while the mitochondria remained mostly intact under hypoxic conditions (Figure S6F). The results demonstrate that under prolonged hypoxic conditions, hepatocellular carcinoma (HCC) cells adapt to the hypoxic environment and significantly increase resistance to sorafenib (SF).

To demonstrate that hypoxia regulates KPNA4-mediated mitochondrial stability to induce SF resistance, MHCC97H cells were overexpressed with KPNA4 under normoxic conditions and silenced under hypoxic conditions. The efficiency of overexpression and silencing was validated through RT-qPCR, and sh-KPNA4-2 (sh-KPNA4) was selected for subsequent experiments (Figure S6G-H). As shown in Fig. 3A-D, overexpression of KPNA4 under normoxic conditions led to increased resistance to SF in MHCC97H cells and a significant decrease in ROS production, while silencing KPNA4 under hypoxic conditions resulted in the opposite trend. Furthermore, the assessment of mitochondrial function confirmed these findings: overexpression of KPNA4 under normoxic conditions decreased mitochondrial content and OCR, increased mitochondrial reduction state, and maintained mitochondrial integrity under SF treatment, while silencing KPNA4 under hypoxic conditions showed the opposite trend (Fig. 3E-J).

In conclusion, under hypoxic conditions, activation of KPNA4 in HCC cells reduces mitochondrial content and maintains its stability, thus promoting SF resistance.

Development of oxygen-generating nanoclusters for enhanced SF sensitivity and photodynamic therapy in hypoxic HCC cells

We have elucidated the mechanism by which hypoxia-induced KPNA4 leads to resistance to SF in HCC. To address the issue of tumor hypoxia, we propose the development of a nanomaterial that can improve tumor oxygenation and enhance the sensitivity of HCC to SF. Additionally, we aim to utilize the enhanced oxygen environment combined with PDT for further reversal of drug-resistant cell growth in HCC. Hb is an endogenous hemoprotein primarily located within red blood cells. Due to its strong oxygen-carrying capacity and small particle size, Hb can penetrate tumor tissue and reach the tumor microenvironment [28]. In this study, Hb is used as an oxygen carrier. ICG is a photosensitizer used in this research. It exhibits high absorption and fluorescence emission peaks in the near-infrared (NIR) region, which allows for the avoidance of interference from visible light during fluorescence imaging. ICG can generate ROS upon laser irradiation, resulting in cellular toxicity [29]. Similarly, the generation of ROS by ICG under laser irradiation requires the conversion of O_2 into ROS in the
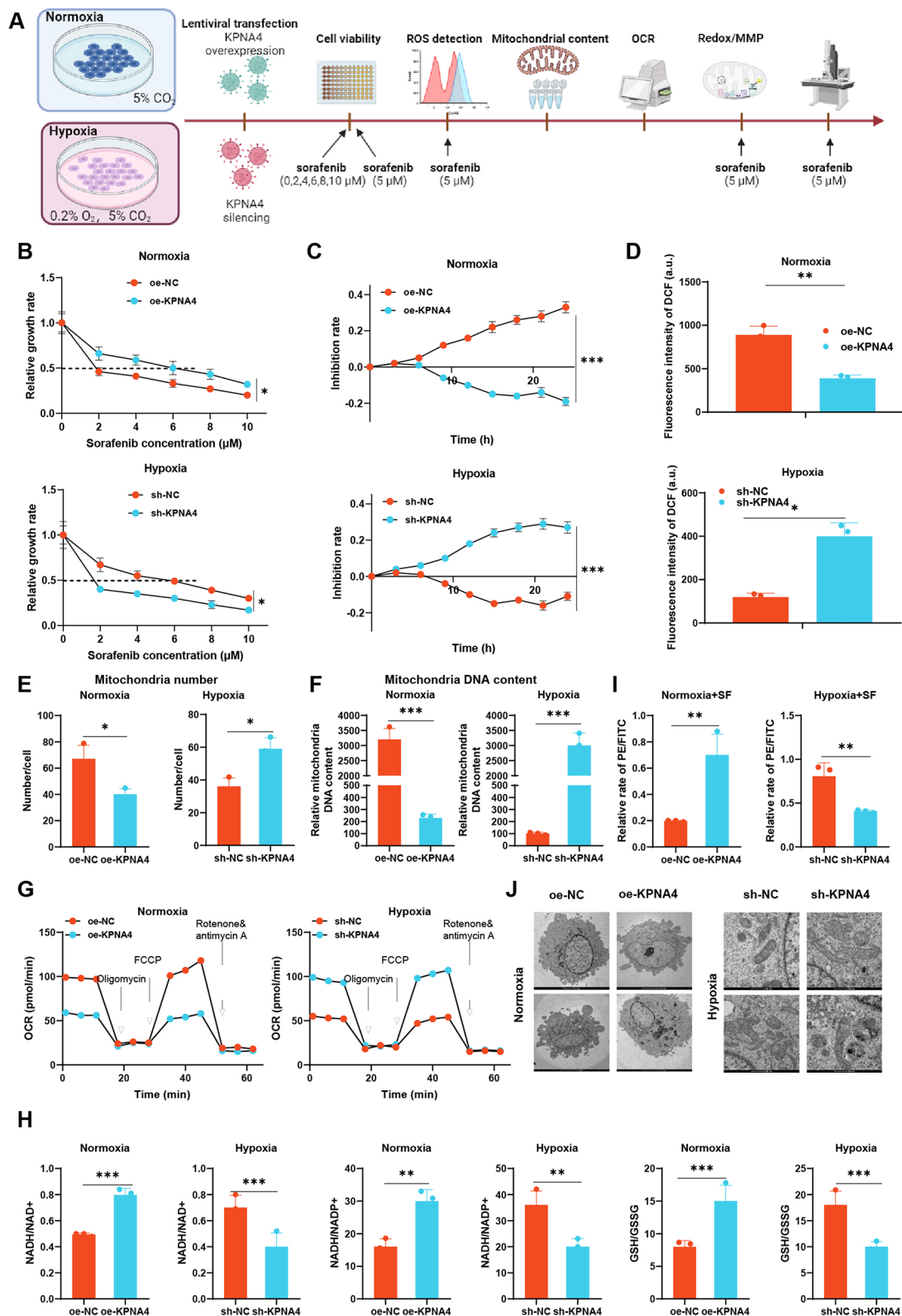
Wang *et al. Journal of Nanobiotechnology*   (2024) 22:473

Page 7 of 25

Fig. 3 (See legend on next page.)

(See figure on previous page.)

Fig. 3 Mechanistic functional validation of hypoxia-regulated KPNA4 mediating SF resistance in HCC cells. Note: (**A**) Experimental procedure illustrating the influence of hypoxia on KPNA4-mediated SF resistance in HCC cells; (**B**) Cell viability of MHCC97H cells in each group after 48 h of SF treatment at different concentrations, measured using CCK-8 assay; (**C**) Time-dependent inhibitory rate of SF-treated (5 µM) MHCC97H cells in different groups, monitored using real-time cell analysis system; (**D**) DCF fluorescence intensity of SF-treated (5 µM) MHCC97H cells in each group, detected by flow cytometry; (**E**-**F**) Quantification of mitochondrial quantity and DNA content in MHCC97H cells in each group, measured by qRT-PCR; (**G**) OCR of MHCC97H cells in each group, analyzed using Seahorse; (**H**) Redox balance monitoring in MHCC97H cells in each group; (**I**) MMP of MHCC97H cells in each group, detected by flow cytometry; (**J**) TEM observation of mitochondrial morphology in MHCC97H cells in each group, scale bar: 5 µM. Cell experiments were performed in triplicate. * indicates a significant difference between two groups, *$P < 0.05$; **$P < 0.01$, ***$P < 0.001$

presence of O_2. Therefore, in our design, Hb serves as an oxygen carrier to improve tumor hypoxia, enhance cell sensitivity to SF by inhibiting KPNA4, and provide an O_2 source for PDT using ICG. The schematic diagram is illustrated in Fig. 4A, with RGD used for targeting αvβ3 receptors on HCC cells [30].

First, ICG was conjugated to Hb through an amide bond to prepare HG. Spectrophotometric analysis revealed a redshift in ICG absorption after binding to Hb, indicating the formation of a chemical bond between the two molecules (Figure S7A). Subsequently, the thiol group of the β-globin subunit was modified with mPEG-MAL or RGD-PEG-MAL to prepare HPG or HPRG, respectively. The modification of PEG improved the material's water solubility and stability, while RGD was used for targeting HCC cells [31]. In addition, HP and HPR were prepared as controls. Gel electrophoresis and MALDI-TOF mass spectrometry analysis confirmed the PEGylation of Hb-NCs (Figure S7B-C). The negatively charged ICG further decreased the Zeta potential of Hb, while the shielding effect of PEG led to an increase in the Zeta potential of Hb molecules, providing additional evidence for the successful conjugation of ICG and PEG to Hb (Fig. 4B). Next, the production of $^1O_2$ by Hb-NCs was evaluated. Under 808 nm laser irradiation, HPG and HPRG exhibited significantly higher levels of $^1O_2$ generation compared to HG, indicating that PEGylation of HG could mitigate self-quenching caused by colloidal instability (Fig. 4C). Furthermore, the oxygen release of Hb-NCs was monitored. Hb-NCs, including Hb, significantly increased the DO level within 250 s, indicating the successful preparation of photosensitized Hb-NCs without compromising the oxygen-carrying capacity of native Hb (Figure S7D).

Furthermore, SF was loaded onto photosensitized Hb-NCs. SF, being hydrophobic, was loaded onto photosensitized Hb-NCs through hydrophobic interactions. The average hydrodynamic diameter of Hb@SF, HG@SF, PG@SF, and HPRG@SF was found to be 230 nm, suitable for intravenous injection. However, only PEGylated HPG@SF and HPRG@SF exhibited complete spherical shapes (Fig. 4D). Furthermore, the stability test results exhibited a similar trend: under various pH conditions and in FBS and human serum, the initial particle size of HPG@SF and HPRG@SF could be maintained over time (Fig. 4E & Figure S7E). Finally, the release of SF from

HPG@SF and HPRG@SF under different pH conditions was evaluated. The results indicated that both HPG@SF and HPRG@SF exhibited sustained SF release, pH-dependent. As pH decreased, the release rate increased (Fig. 4F), possibly due to SF being a hydrophobic drug [32], leading to increased solubility at acidic pH [33, 34], thereby reducing the hydrophobic interactions between SF and photosensitized Hb-NCs. Moreover, considering the acidic environment of tumor tissues, this would result in higher drug release in the tumor microenvironment, enhancing the efficacy against HCC.

The above results demonstrate the successful construction of Hb-NCs with excellent oxygen generation capabilities and the organic loading of ICG and SF.

Enhanced Cellular Uptake and SF Resistance reversal by HPRG@SF

The next step involved validating the targeting efficacy of HPRG@SF on HCC cells and its impact on SF resistance. Existing research demonstrated that MHCC97H cells highly express the αvβ3 receptor [30]. After treating the MHCC97H cells with different groups, the uptake of HPRG@SF by the cells was detected using ICG fluorescence. The experimental workflow for material uptake in both the monolayer and spherical HCC cell models is illustrated in Fig. 5A. CLSM observations revealed that HPRG@SF was more readily taken up by MHCC97H cells compared to HPG@SF and free ICG solution. Furthermore, when incubated with MHCC97H cells, the presence of free RGD and HPRG@SF led to a significant decrease in ICG fluorescence signal, indicating that RGD could compete with HPRG@SF for binding to the αvβ3 receptor on MHCC97H cells (Fig. 5B). The findings from flow cytometry analysis further supported the observations made using CLSM (Fig. 5C). Additionally, we established a spherical cell model of MHCC97H cells to evaluate the penetration of HPRG@SF. It was discovered that compared to the free ICG solution, both HPRG@SF and HPG@SF exhibited strong penetration, with HPRG@SF showing more significant effects. Moreover, the presence of free RGD inhibited the penetration of HPRG@SF, providing further confirmation of the CLSM observations (Fig. 5D).

Subsequently, the effects of Hb-NCs on alleviating SF resistance were investigated by examining whether it could improve hypoxia and inhibit KPNA4. First, low

oxygen levels were detected using the hypoxia detection reagent (HG), and the expression of hypoxia factor HIF-1α was determined through immunofluorescence staining. The results indicated that regardless of normoxia or hypoxia conditions, treatment with Hb-NCs significantly reduced HG fluorescence and the expression of HIF-1α in MHCC97H cells, suggesting that Hb-NCs effectively improved cellular hypoxia (Fig. 5E-F). Furthermore, to validate the reversal of SF-induced upregulation of KPNA4 by Hb-NCs, mitochondria function analysis was performed on hypoxia-cultured MHCC97H cells treated with SF-free Hb-NCs. Western blot analysis revealed that compared to the Control group, Hb-NCs significantly reduced the expression of HIF-1α and KPNA4 (Fig. 6A). Moreover, after treatment with all Hb-NCs formulations, the resistance of MHCC97H cells to SF decreased, and the production of ROS significantly increased (Fig. 6B-D). Mitochondria function analysis further confirmed these findings, showing an increase in mitochondrial content and oxygen consumption rate in MHCC97H cells after treatment with all Hb-NCs formulations. Additionally, the mitochondrial redox state decreased (Fig. 6E-H). Furthermore, in the presence of SF treatment, the MMP decreased, and mitochondrial cristae exhibited partial disintegration (Fig. 6I-J).

In summary, HPRG@SF effectively achieved cellular uptake by targeting the αvβ3 receptor that is highly expressed on MHCC97H cells, thereby improving cellular hypoxia through the oxygen-carrying function of Hb, inhibiting the expression of KPNA4 and inducing sensitivity to SF in MHCC97H cells.

Synergistic Antitumor effects of HPRG@SF-Mediated PDT on HCC cells

In the previous section, it was mentioned that ICG can generate ROS under laser irradiation, resulting in cytotoxicity to cells. Therefore, we conducted further verification in vitro to confirm if ICG-mediated PDT could enhance the suppression of SF resistance in HCC cells. Firstly, the ability of ICG-conjugated Hb-NCs to generate ROS under laser irradiation was verified using CLSM and flow cytometry. The experimental procedure is illustrated in Fig. 7A. As shown in Fig. 7B-C, in the absence of laser irradiation, there was no significant change in the DCF fluorescence intensity, indicating no significant alteration in ROS levels in the MHCC97H cells of all groups. However, after laser irradiation, except for the Control group, a significant increase in ROS levels was observed in MHCC97H cells in all other groups. Among them, the HPG and HPRG groups exhibited a more pronounced increase in ROS levels due to the internalization of the materials by the cells. Notably, the HPRG group, which contained a targeting peptide RGD, showed the most prominent increase.

Next, to further investigate the cytotoxicity of HPRG@SF-mediated SF targeted therapy combined with PDT on hypoxic HCC in vitro, cell viability was evaluated in MHCC97H cells treated with different ICG concentrations with or without laser irradiation. The results showed that under laser non-irradiation, there was no significant change in cell viability in the ICG, HPG, and HPRG groups at various ICG concentrations. However, in the SF+ICG, HPG@SF, and HPRG@SF groups, cell viability gradually decreased with increasing ICG concentration due to the addition of SF. Among them, the cell viability in the SF+ICG group was higher than that in the HPG@SF and HPRG@SF groups, which could be attributed to the oxygen-carrying effect of Hb improving the hypoxic environment. Under laser irradiation, cell viability in all six groups decreased with increasing ICG concentration, with the SF+ICG group showing the most significant decrease, especially in the HPG@SF and HPRG@SF groups (Fig. 7D & Figure S8A-B). The combined indexes in the combination groups were further calculated, which showed that at 24 h of material treatment, HPG@SF and HPRG@SF exhibited certain synergistic effects, while free ICG combined with free SF treatment did not show obvious synergistic effects, consistent with our cell viability detection results. Moreover, after 48 h of treatment, only HPRG@SF showed synergistic effects, benefiting from the targeting effect of RGD (Fig. 7E & Figure S8C).

Subsequently, the antitumor efficacy was validated in an MHCC97H spheroid model, which has more pathological and physiological relevance compared to monolayer culture models (Fig. 7F). The results showed that under laser non-irradiation, the volume of cell spheroids decreased slightly in the SF group and SF+ICG group while significantly decreasing in the HPG@SF and HPRG@SF groups. Under laser irradiation, the SF group showed a slight decrease in spheroid volume, while the groups containing ICG (ICG, HPG, HPBG, and SF+ICG) showed a significant decrease, with the HPG and HPBG groups exhibiting a more pronounced decrease due to the oxygen supply from Hb to ICG. Compared to other groups, the HPG@SF and HPRG@SF groups showed a more significant decrease, which could be attributed to the combined effect of SF treatment and PDT. However, the effect was more pronounced in the HPRG@SF group due to its targeting effect (Fig. 7G).

The above results demonstrate that Hb can both improve the hypoxic tumor environment and provide an oxygen source for ROS generation by ICG. Therefore, HPRG@SF-mediated combined application of SF and PDT shows effective tumor cell-killing ability in vitro.
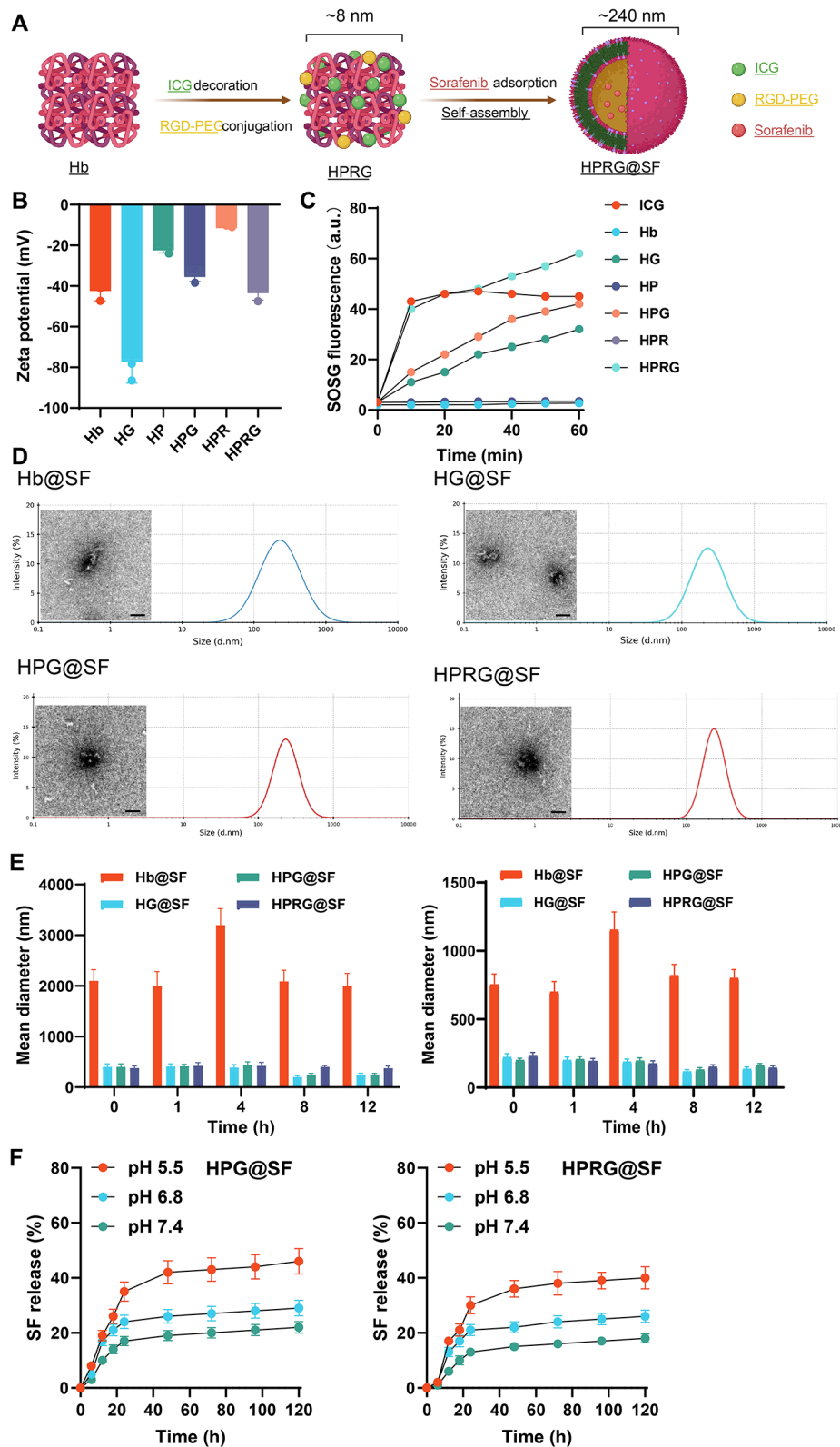
Fig. 4 Characterization of HPRG@SF. Note: (**A**) Schematic representation of HPRG@SF synthesis; (**B**) Zeta potential of Hb-NCs aqueous solutions detected by DLS; (**C**) Determination of $^1O_2$ generation efficiency by measuring the fluorescence intensity of SOSG reagent; (**D**) Size distribution and morphology of each Hb-NCs determined by DLS and TEM analysis, scale bar: 100 μm; (**E**) **a**. Colloidal stability of each Hb-NCs loaded with SF in FBS detected by DLS; **b**. Stability of each Hb-NCs loaded with SF in human serum detected by DLS, experiment repeated three times; (**F**) Dialysis method to detect the release of SF from HPG@SF and HPRG@SF under different pH conditions. Experiment repeated three times
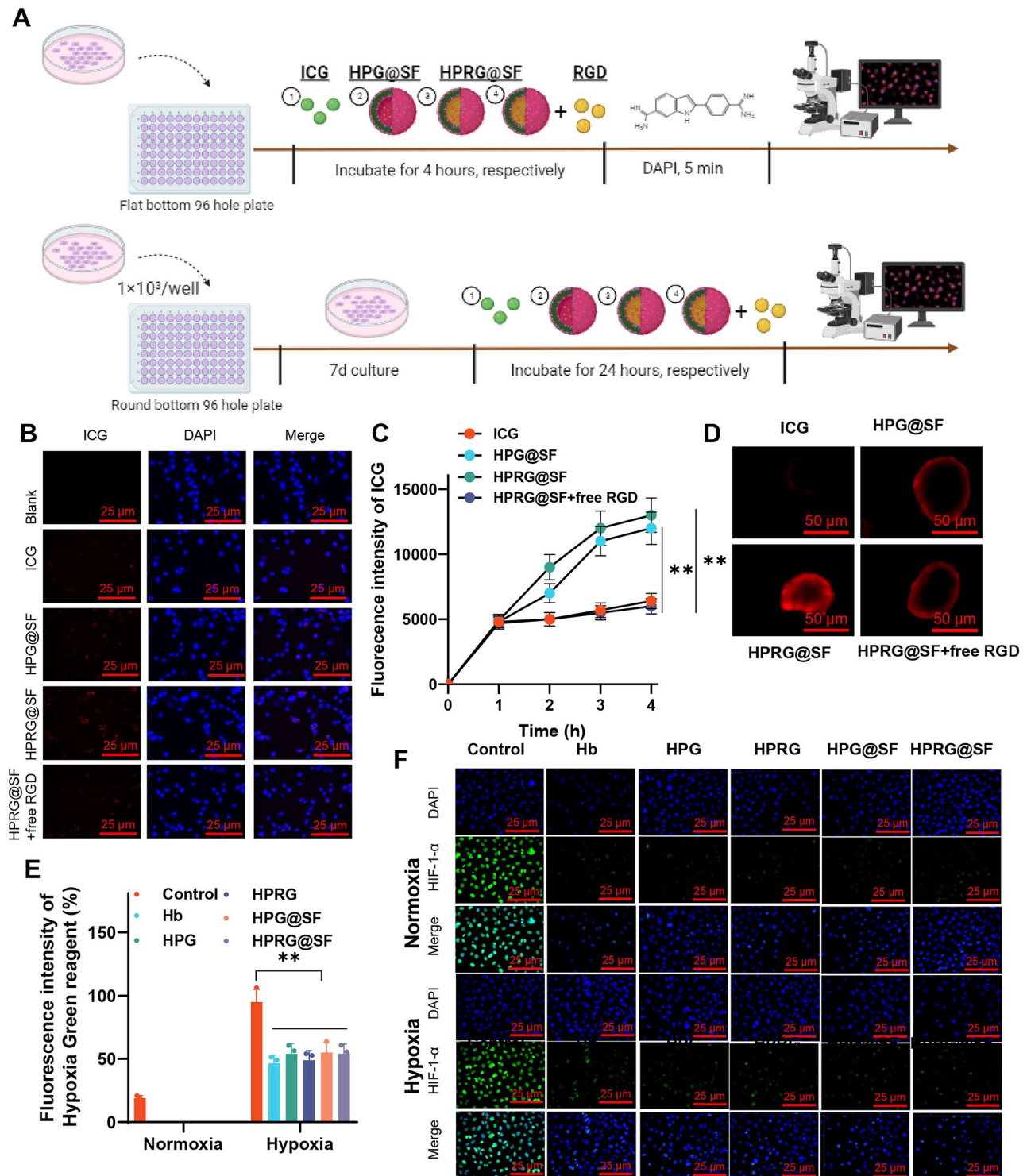
Fig. 5 Validation of the active targeting effect of HPRG@SF on HCC cells. Note: (**A**) Experimental workflow for the uptake of materials by monolayer and spheroid HCC cells; (**B**) CLSM observation of the uptake of various materials by MHCC97H cells, scale bar: 20 μm; (**C**) Flow cytometry detection of the fluorescence intensity of ICG in MHCC97H cells in each group; (**D**) CLSM observation of the uptake of various materials by MHCC97H spheroid cells, scale bar: 200 μm; (**E**) Flow cytometry detection of the fluorescence intensity of the azo-cleaved HG reagent in MHCC97H spheroid cells to reflect intracellular hypoxia; (**F**) Immunofluorescence staining to detect the expression level of HIF-1α in MHCC97H cells in each group, scale bar: 20 μm. Cell experiments were repeated three times. * indicates a significant difference between the two groups, **$P < 0.01$
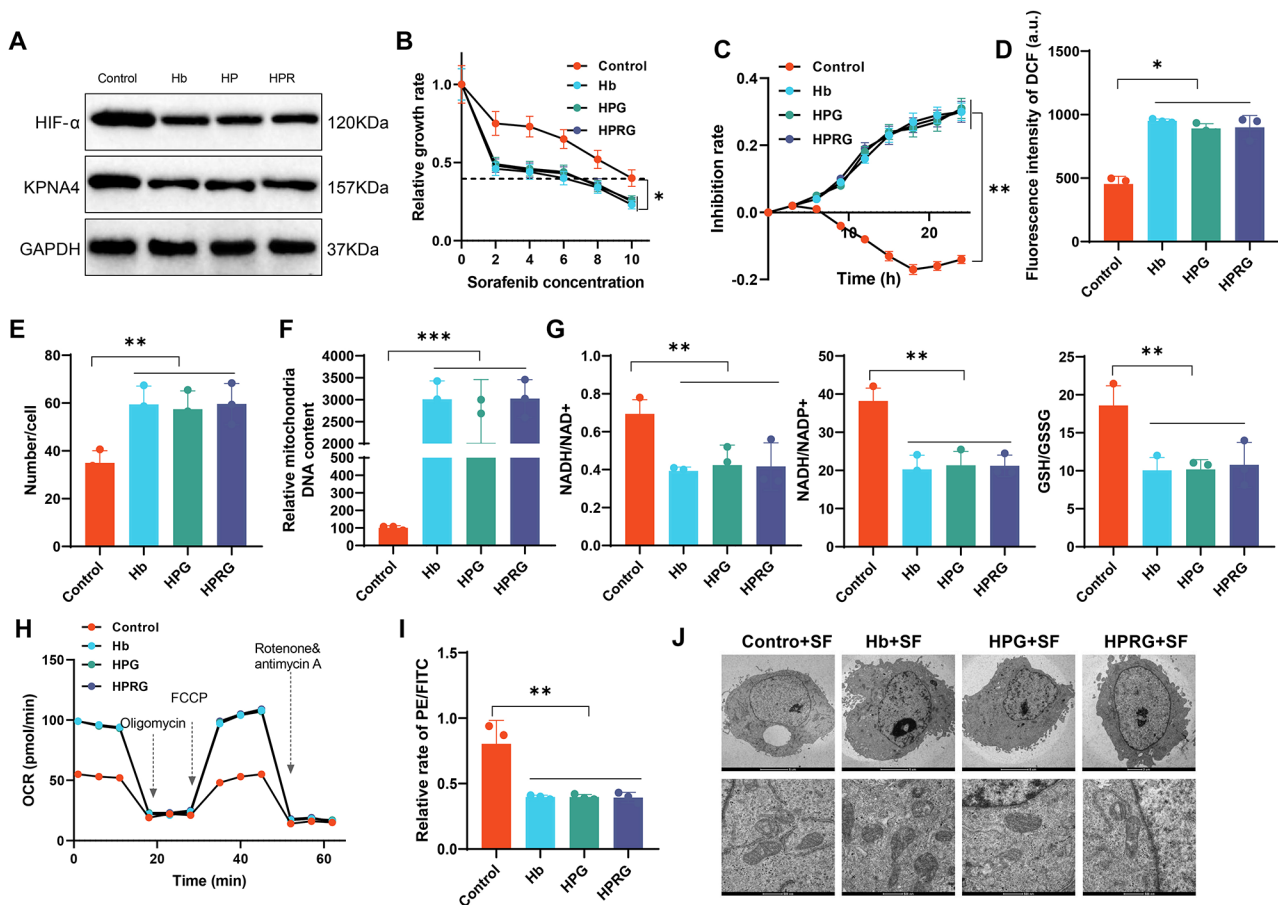
Fig. 6 Effects of Hb-NCs on the function of hypoxic MHCC97H cells mediated by KPNA4. After incubating the cell groups with MHCC97H cells for 4 h, (**A**) Western blot was used to detect the protein expression levels of HIF-1α and KPNA4 in MHCC97H cells of each group; (**B**) CCK-8 assay was used to measure the cell viability of MHCC97H cells in each group after 48 h of treatment with different concentrations of SF; (**C**) Real-time cell analysis system was used to monitor the inhibition rate of MHCC97H cells in each group over time after treatment with 5 µM of SF; (**D**) Flow cytometry was used to measure the DCF fluorescence intensity in MHCC97H cells of each group; (**E-F**) qRT-PCR was used to measure the mitochondrial count and DNA content in MHCC97H cells of each group; (**G**) Oxidation-reduction balance in MHCC97H cells of each group was monitored; (**H**) Seahorse analysis was used to detect the OCR of MHCC97H cells in each group; (**I**) Flow cytometry was used to measure the MMP of MHCC97H cells in each group; (**J**) TEM was used to observe the mitochondrial morphology of MHCC97H cells in each group, scale bar: 5 µm; (**K**) Schematic diagram illustrating the mitigation of hypoxia-induced mitochondrial dysfunction by Hb-NCs. Cell experiments were repeated three times. * indicates a significant difference between two groups, *$P < 0.05$; **$P < 0.01$, ***$P < 0.001$

Enhanced Antitumor Efficacy and Tumor Targeting of HPRG@SF in vivo

Finally, the antitumor efficacy of HPRG@SF was validated in vivo. Initially, subcutaneous tumor-bearing nude mice were established by subcutaneous injection of anaerobically cultured MHCC97H cells. The biodistribution of HPRG@SF was evaluated using NIR imaging, aided by the excellent NIR fluorescent properties of ICG. In vivo imaging was performed within 24 h after intravenous injection of the materials, and after 24 h, major organs and tumors were dissected for ex vivo imaging. The results showed that within 24 h, the fluorescence signals of the SF+ICG group, HPG@SF group, and HPRG@ SF group were predominantly located in the kidneys and tumor tissues. The minimal accumulation in the liver and lungs indicated that the polyethylene glycol-modified

Hb particles could degrade into individual protein molecules circulating in the blood. The SF+ICG group, due to the non-targeting nature and smaller particle size of ICG, was quickly metabolized by the kidneys, leading to a gradual decrease in tumor accumulation. In contrast, the tumor fluorescence signal in the HPG@SF and HPRG@ SF groups lasted longer, with the HPRG@SF group exhibiting the strongest intensity. This extended accumulation at the tumor site was attributed to its targeting capability, resulting in prolonged retention time in the tumor region (Fig. 8A-B). Subsequently, tumor tissues were sliced and observed under a microscope. The results revealed minimal fluorescence in the tumor tissues of the HPG@ SF group, possibly due to passive targeting by the nanomaterials. In contrast, abundant ICG fluorescence was
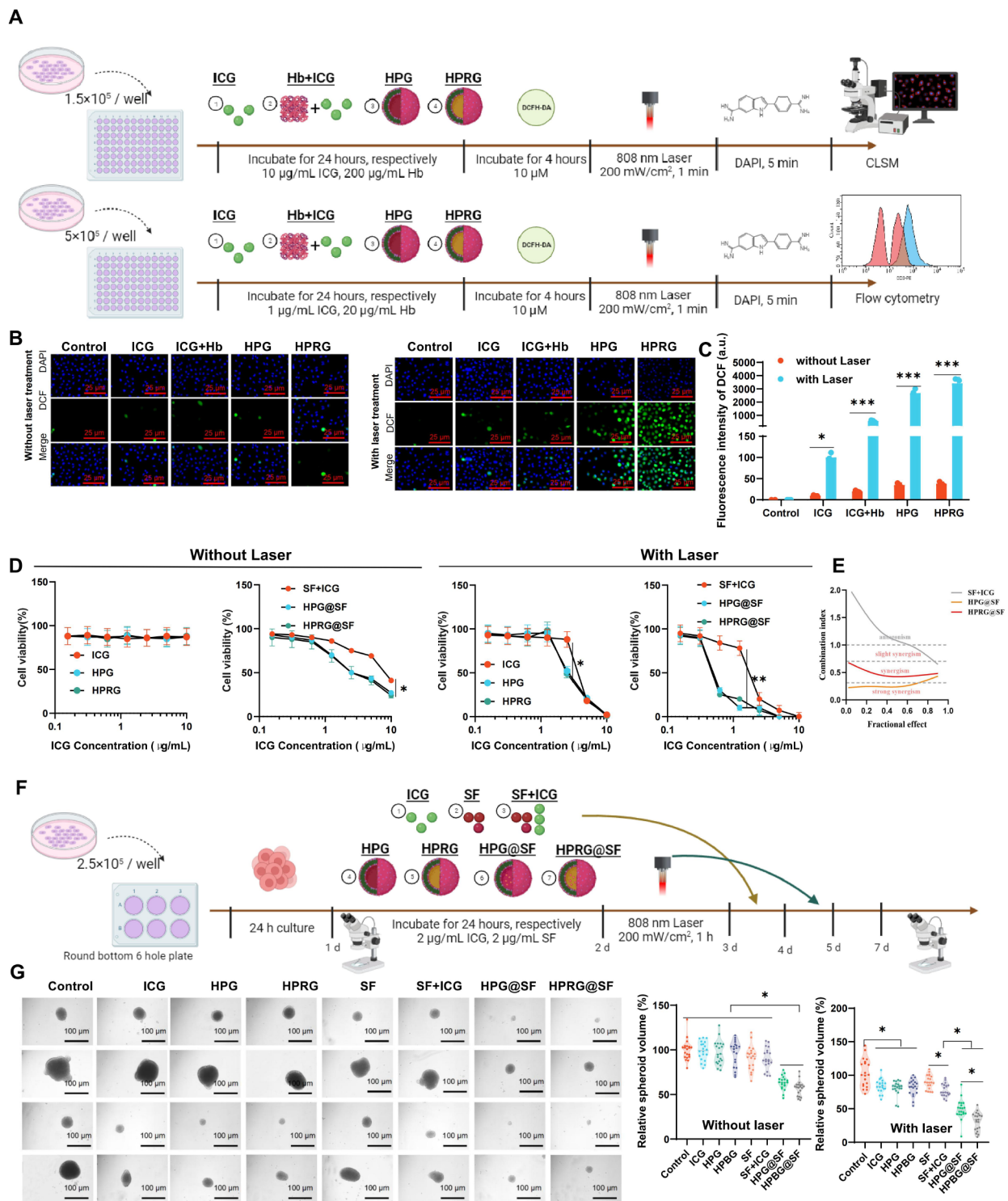
Fig. 7 Effects of HPRG@SF on improving hypoxic conditions and combined PDT on SF resistance of HCC cells. Note: (**A**) Experimental flowchart for observing and detecting ROS production using CLSM and flow cytometry; (**B**) CLSM observation of DCF fluorescence in MHCC97H cells of each group; (**C**) Flow cytometry measurement of DCF fluorescence intensity in MHCC97H cells of each group; (**D**) CCK-8 assay to measure the cell viability of MHCC97H cells in each group after 48 h of treatment with ICG materials of different concentrations; (**E**) Fitting of the combined index curve based on the relationship between cell toxicity and treatment in each group; (**F**) Experimental flowchart for in vitro toxicity of MHCC97H cell spheroid model cultured in pellets; (**G**) Brightfield images of spheroids in each grid, scale bar: 500 μm. Cell experiments were repeated three times. * indicates a significant difference between two groups, *$P < 0.05$; **$P < 0.01$, ***$P < 0.001$
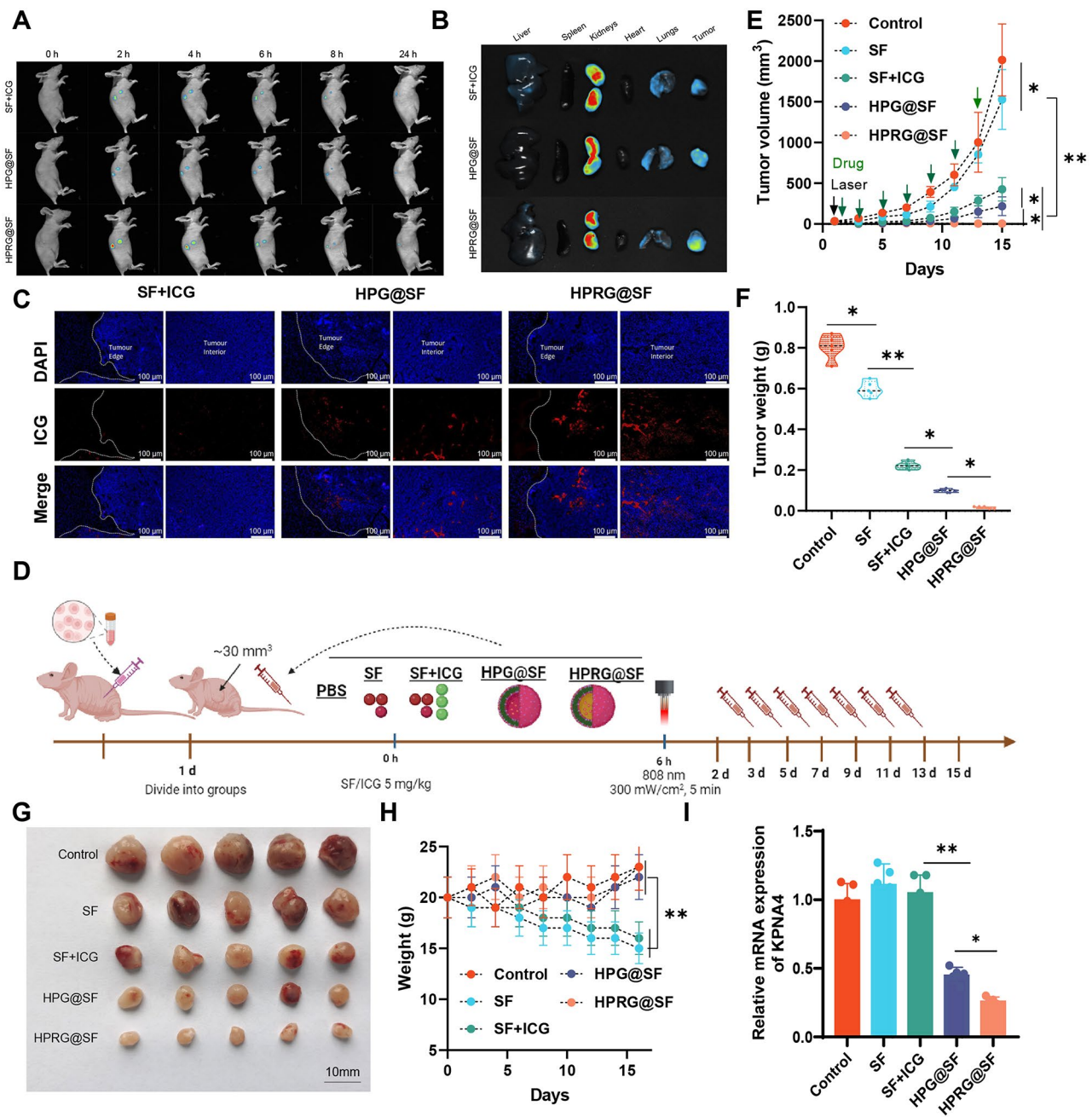
Fig. 8 In vivo validation of HPRG@SF's regulation on hypoxia-resistant HCC cells in SF. Note: (**A**) NIR fluorescence imaging of the fluorescent distribution in tumor-bearing nude mice in each group; (**B**) NIR fluorescence imaging of the fluorescent distribution in major organs and tumor tissue in nude mice in each group; (**C**) Tumor volume changes in tumor-bearing nude mice in each group; (**D**) Flowchart of in vivo anti-tumor experiment with HPRG@SF; (**E**) White light images of tumors in tumor-bearing nude mice in each group; (**F**) Tumor weight in tumor-bearing nude mice in each group; (**G**) Changes in body weight of tumor-bearing nude mice in each group; (**H**) CLSM observation of the fluorescence distribution in tumors of tumor-bearing nude mice in each group; (**I**) RT-qPCR detection of KPNA4 expression levels in tumors of tumor-bearing nude mice in each group. Fluorescence imaging was performed on three nude mice in each group, and treatment detection was performed on five nude mice in each group. *$P < 0.05$; **$P < 0.01$

observed in the tumor tissues of the HPRG@SF group, indicating its effective active targeting ability (Fig. 8C).

Following this, tumor-bearing nude mice were treated with different materials to verify the in vivo antitumor activity, as shown in Fig. 8D. As demonstrated in Fig. 8E-G, compared to the Control group, the SF group

exhibited a slightly reduced tumor growth rate and volume after treatment. The SF+ICG group displayed significantly decreased tumor growth rate and volume compared to the SF group. Moreover, both the HPG@ SF group and HPRG@SF group exhibited significantly reduced tumor growth rate and volume compared to

the SF+ICG group, with the HPRG@SF group showing the most prominent trend. Additionally, the pathological staining results of the tumor tissues were consistent with the trends in tumor volume among the groups (Figure S9). Subsequently, the body weight of the mice in each group was measured, and major organs and tumor tissues were collected for hematoxylin and eosin (H&E) staining after the treatment. It was found that the body weight of mice in the SF group and SF+ICG group significantly decreased, while there was no significant change in the body weight of mice in the HPG@SF group and HPRG@SF group. According to the H&E staining results, no significant pathological changes were observed in the major organs. However, the white blood cell count decreased significantly in the SF group and SF+ICG group, whereas there was no significant decrease in the white blood cell count of mice in the HPG@SF group and HPRG@SF group (Fig. 8H & Figure S9 & Table S1), indicating that HPRG@SF exhibited good biocompatibility. Finally, the expression of KPNA4 in tumor tissues was examined, confirming that only the HPG@SF group and HPRG@SF group downregulated KPNA4 expression through Hb-mediated oxygen transport (Fig. 8I).

In conclusion, HPRG@SF primarily accumulated in tumor tissues exhibited good biocompatibility and effectively inhibited the growth of in vivo HCC drug-resistant cells by improving tumor hypoxia and reducing KPNA4 expression in combination with enhanced PDT.

Discussion

HCC is a highly malignant tumor that presents a significant challenge in treatment [35–37]. Hypoxic environments play a crucial role in the development of HCC and have been shown to contribute to the emergence of drug resistance in tumor cells [38–40]. The formation of hypoxic environments is primarily attributed to insufficient blood supply in tumor tissue and the increased oxygen demand of rapidly growing tumor tissue [41–43]. Previous studies have indicated a close correlation between hypoxic environments and prognosis in HCC patients, as well as resistance to initial tumor treatments [44]. Thus, blocking hypoxic environments holds crucial significance in improving HCC treatment outcomes [45, 46].

In this study, we explored the mechanisms of HCC resistance to SF from the perspective of the hypoxic microenvironment, employing the innovative methods of Hb-NCs and PDT. Compared to previous studies, our research exhibits notable innovation. Firstly, we highlight the significant impact of hypoxic environments on HCC drug resistance and conduct subsequent research based on this insight. Secondly, we utilize the approach of Hb NC and PDT to enhance SF sensitivity by targeting the hypoxic environment within the tumor. Such a

combination therapy strategy provides new ideas and strategies for HCC treatment.

In this study, through scRNA-seq and gene co-expression network analysis, we discovered the role of the hypoxia-regulated key factor KPNA4 in HCC. KPNA4 is upregulated in hypoxic conditions and closely associated with SF resistance in HCC. Further research revealed that KPNA4 affects the expression of a series of genes related to drug resistance in tumor cells by regulating transcription factors. Compared to previous studies, our results reinforce the association between hypoxic environments and HCC drug resistance and identify KPNA4 as an important regulatory factor.

The Hb NC employed in this study plays a significant role in alleviating hypoxic environments and suppressing KPNA4 expression. The preparation method and characterization results demonstrate that Hb-NCs possess excellent capability in mitigating hypoxic environments, and they can inhibit KPNA4 expression through specific reactions. Compared to other nanoparticle drug delivery systems, Hb-NCs offer the advantages of simple preparation, good stability, and high biocompatibility. These characteristics present the potential application prospects of Hb-NCs in HCC treatment.

The results of the in vivo animal experiment demonstrate the specific targeting of tumor tissues by the use of a hemoglobin nanocluster composite. Compared to conventional treatment methods, hemoglobin nanoclusters composite exhibit superior efficacy in inhibiting tumor growth and spread, thereby enhancing therapeutic outcomes. This observed effect aligns with anticipated results and may be attributed to the alleviation of hypoxic environments by hemoglobin nanoclusters and the suppression of KPNA4 expression.

Conclusion

In summary, preliminary conclusions can be drawn as follows: hypoxia can promote HCC cell resistance to SF by upregulating KPNA4 to reshape mitochondrial function, and the prepared HPRG@SF actively targets HCC by improving the tumor's hypoxic microenvironment through oxygen transport by Hb, thus enhancing SF sensitivity, and combined with enhanced PDT, further inhibiting drug-resistant HCC cell growth (Fig. 9).

The results of this study reveal the significant impact of the hypoxic microenvironment on HCC drug resistance and propose an innovative strategy based on Hb NC and PDT. This approach helps enhance treatment outcomes and address drug resistance caused by hypoxic environments. The scientific value of this research primarily lies in several aspects. Firstly, by extracting HCC-related scRNA-seq data from the GEO database, we explore the differentially expressed genes in malignant cells under hypoxic conditions and identify KPNA4 as a potential key
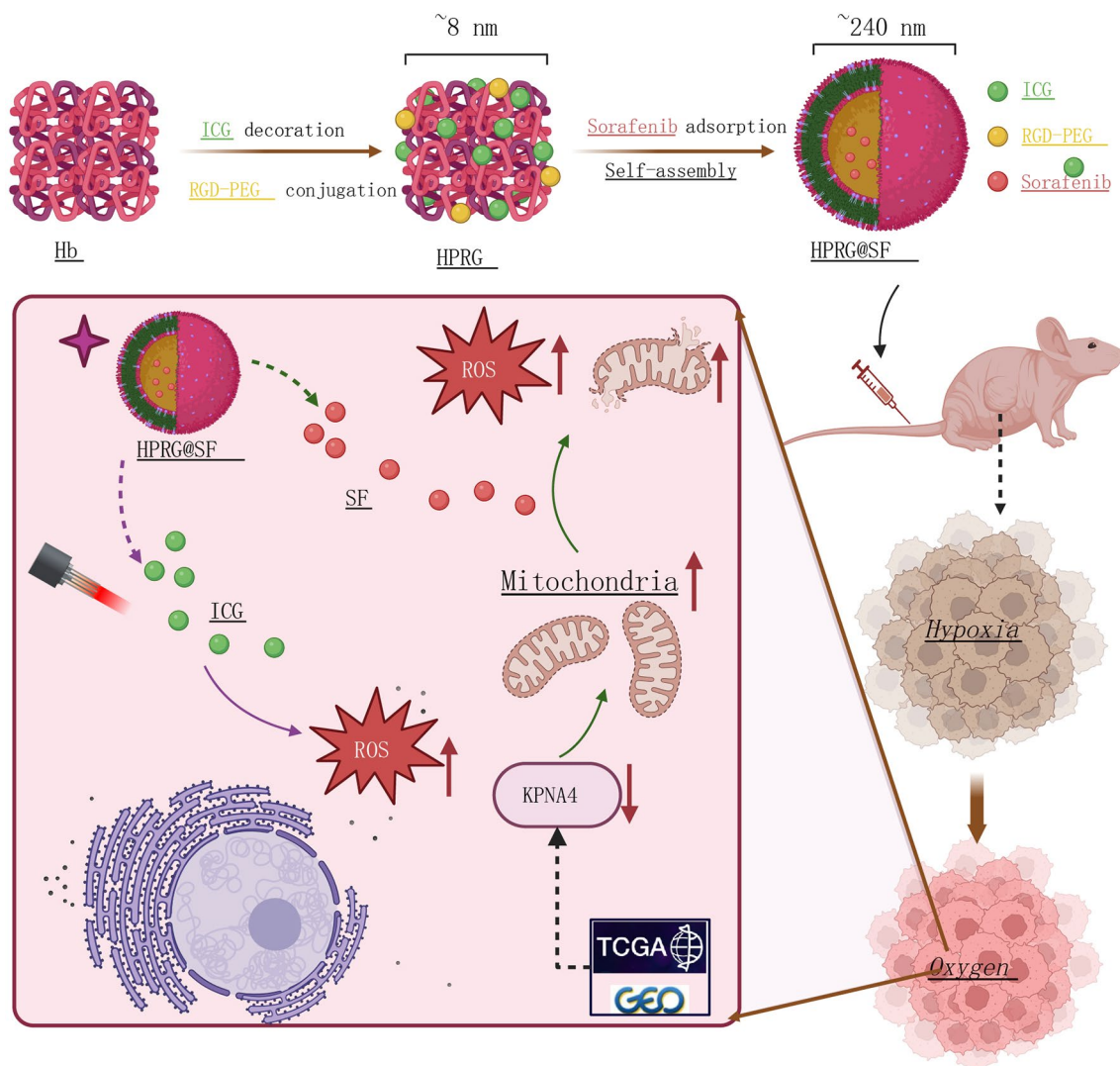
Fig. 9 Schematic diagram illustrating the modulation of the hypoxic tumor microenvironment by Hb nanoclusters co-loaded with ICG and SF via KPNA4 regulation, thereby enhancing the combination of photodynamic and targeted therapy for HCC

factor mediating HCC resistance to SF in a hypoxic setting. This finding not only provides new targets for HCC treatment under hypoxic conditions but also establishes a theoretical basis for understanding drug resistance in other tumor types associated with hypoxic environments. Secondly, Hb NC is prepared and loaded with ICG and SF to obtain HPRG@SF. The research results demonstrate that HPRG@SF exhibits excellent targeting capability and effectively suppresses KPNA4 expression by improving hypoxic environments, thereby enhancing the therapeutic efficacy of SF. Additionally, HPRG@SF can cause the death of hypoxic HCC cells through the combination of PDT and enhanced PDT. This finding not only offers a novel treatment strategy but also provides new insights into the application of PDT in tumor therapy. The clinical value of this study lies in the validation through in vivo animal experiments, which demonstrate

that HPRG@SF can suppress the resistance of hypoxic HCC cells to SF by improving the hypoxic environment in combination with PDT. These research findings provide new treatment options and ideas for clinical HCC patients, with the potential to improve the effectiveness of drug treatment, prolong patient survival, and alleviate suffering.

However, this study has some limitations. Firstly, the experimental results are mainly based on in vitro cell experiments and in vivo animal experiments, and they have not been validated in clinical practice. Therefore, further clinical trials are needed to verify the therapeutic efficacy and safety of HPRG@SF in HCC. Secondly, this study only explores the mechanism of hypoxic environments in HCC drug resistance, and other factors, such as the cell cycle and gene mutations that affect treatment outcomes, require further investigation. Although

our study shows the potential of HPRG@SF in treating hypoxic HCC, treatment plans still need refinement and optimization. Future research can incorporate other treatment modalities, such as chemotherapy and immunotherapy, to further enhance treatment outcomes. Moreover, more clinical trials can be conducted for different subtypes and stages of HCC to determine the adaptability and efficacy of HPRG@SF in different patients and explore the possibility of personalized therapy. Finally, further in-depth research is needed to elucidate the mechanism of drug resistance in hypoxic HCC in order to identify more treatment targets and strategies.

Materials and methods
scRNA-seq data download
In this study, scRNA-seq data related to HCC were obtained using the Gene Expression Omnibus (GEO, https://www.ncbi.nlm.nih.gov/geo/) database. The dataset used for analysis was GSE202642 [47]. A total of seven samples of adjacent normal tissues (GSM6127499, GSM6127500, GSM6127501, GSM6127502, GSM6127503, GSM6127504, GSM6127505) and four samples of HCC tissues (GSM6127506, GSM6127507, GSM6127508, GSM6127509) were selected. Due to the use of publicly available data, ethical approval and informed consent were not required for this study.

scRNA-seq cell annotation
In the bioinformatics analysis, the scRNA-seq data underwent standard preprocessing steps using the R package "Seurat". Firstly, genes that appeared in less than three cells were removed, and cells with less than 200 genes were excluded. Additionally, a limit of mitochondrial gene proportions not exceeding 10% was set. Next, data normalization was performed using the LogNormalize method. Cell clustering analysis was conducted using the "FindClusters" function, and the clustering results were visualized using the "RunUMAP" function. Furthermore, the "FindMarkers" function was used to compare cells in specific clusters with all other cells using the Wilcoxon rank-sum test, determining differentially expressed genes. Bonferroni correction was applied, using a significance threshold of $P<0.05$ to identify statistically significant differentially expressed genes. Finally, known cell lineage-specific marker genes were referenced, and cell types were annotated using CellMarker [48].

Extraction of malignant cells in scRNA-seq data
Initially, the subset function was used to extract epithelial cells from the samples, followed by CNV analysis using the inferCNV package. Subsequently, non-malignant cells were removed from the epithelial cells using the K-means algorithm, and UMAP clustering analysis was performed on the malignant cells. To assess the hypoxia status across different malignant cell subtypes, we utilized the "hypoxia" related dataset from the GSEA database (Table S2). The AddModuleScore function and the AuCell function were employed to score the hypoxia condition in different malignant cell subgroups [49].

Selection of Differentially Expressed Genes in Hypoxic Cells in scRNA-seq Data
Differential expression gene screening was conducted using the "limma" package in R. By applying a significance threshold of $P<0.05$, we identified differentially expressed genes in both high and low hypoxia score malignant cell clusters. A volcano plot depicting the differentially expressed genes was created using the "ggplot2" package in R [50].

Bulk RNA-seq data download
We downloaded the transcriptome data for 374 patients with HCC from The Cancer Genome Atlas (TCGA) database (https://portal.gdc.cancer.gov/). These samples included both adjacent normal tissues and HCC tissues. Additionally, we obtained clinical information for 377 patients, including time, fustat, stage, and T. Additionally, we retrieved several relevant transcriptome sequencing datasets from the GEO database, including the GSE14520 dataset for HCC tissues and adjacent normal tissues, the GSE41666 dataset for HCC cells under normoxic and hypoxic conditions, the GSE189711 dataset for SF-sensitive and SF-resistant HCC cells, and the GSE225537 dataset for HCC cells before and after SF treatment [51]. Basic information about these datasets is provided in Table S3. Since our data is sourced from public databases, our study does not involve ethical approval or informed consent.

Differential Gene expression analysis of bulk RNA-seq data
We performed differential gene expression analysis on the various transcriptome datasets from the TCGA and GEO databases. The analysis was conducted using the "limma" package in the R programming language, with the false discovery rate (FDR) correction applied to adjust the significance of the differential P-values. The selection criterion was set as $P<0.05$, resulting in the identification of differentially expressed genes. To visualize these genes, we utilized the "ggplot2" package and created volcano plots [50].

Weighted Gene Co-expression Network Analysis (WGCNA)
WGCNA analysis was performed on the GSE14520 dataset. The WGCNA package was used to identify biologically meaningful modules of gene co-expression in high-throughput data and explore pairwise correlations between genes. The analysis consisted of the following steps: construction of the gene co-expression network,

module identification, analysis of module interrelationships, and selection of highly correlated genes [52]. A soft-thresholding method was employed to better adhere to the scale-free topological features when constructing the gene co-expression network. The soft-thresholding parameter was set to $\beta = 6$, scale-free $R^2 = 0.90$, and the height cut-off was set at 0.25.

Clinical correlation analysis in the TCGA-LIHC dataset

ROC analysis was conducted on the data using the pROC package, and the results were visualized using the ggplot2 package. Proportional hazard assumption testing and survival regression were performed using the survival package. The survminer and ggplot2 packages were utilized to visualize the results. Spearman analysis was used to assess the correlation between KPNA4 and HIF-1α, and the results were visualized using the ggplot2 package [53].

Cell Culture and Hypoxia Treatment

Human HCC cell lines, Huh7 (CL-0120, Procell, Wuhan, China), MHCC97H (17,495), and MHCC97L (2999, Biofeng, Shanghai, China), as well as human kidney epithelial cells, HEK293T (CL-0005, Procell), were purchased. Huh7, MHCC97L, and HEK293T cells were cultured in DMEM medium (12,491,015, Thermofisher) containing 10% FBS (A5669701, Thermofisher), 10 μg/mL of streptomycin, and 100 U/mL of penicillin (V900929, Sigma, USA). MHCC97H cells were cultured in a high glucose DMEM medium (11,965,092, Thermofisher) [54].

Normoxic/Hypoxic Treatment Groups: (1) Normoxic group - HCC cells were cultured in a humidified CO_2 incubator with 5% CO_2 (Heracell™ Vios 160i CR CO_2 incubator, 51,033,770, Thermo Scientific™, Germany); (2) Hypoxic group - HCC cells were cultured in a humidified incubator with 0.2% O_2 and 5% CO_2 [55].

Lentivirus production and cell transfection

Potential short hairpin RNA (shRNA) target sequences for KPNA4 were analyzed based on GenBank cDNA sequences. Two target sequences for KPNA4 were designed, with one serving as a negative control without a knockdown sequence (sh-NC). The primer sequences are provided in Table S4 and were synthesized by GenePharma® (Shanghai, China). Lentiviral packaging system was constructed using pLKO.1 (lentiviral gene silencing vector). The packaging virus and target vector were co-transfected into HEK293T cells using Lipofectamine 2000 (11,668,500, Thermofisher) when cells reached 80–90% confluency. The supernatant was collected 48 h after culture, filtered and subjected to centrifugation to obtain viral particles. The collected virus at the exponential growth phase was used to determine viral titers. The overexpression lentivirus was constructed and packaged by Genechem Ltd (Shanghai, China), using LV-KPNA4 as the lentiviral overexpression vector.

When MHCC97H cells were in a logarithmic growth phase, they were digested with trypsin and resuspended to a concentration of 5×10^4 cells/mL, and then seeded in a 6-well plate with 2 mL per well. Prior to establishing the in vitro cell model, each lentivirus (MOI=10, viral titer 1×10^8 TU/mL) was added to the cell culture medium and incubated for 48 h. Stable cell strains were selected using 2 μg/mL puromycin (UC0E03, Sigma-Aldrich, Germany) for 2 weeks [56].

The cell transfection groups were as follows: (1) sh-NC group - transfected with lentivirus constructed from the negative control knockdown vector; (2) sh-KPNA4-1 group - transfected with lentivirus constructed from sh-KPNA4-1 vector; (3) sh-KPNA4-2 group - transfected with lentivirus constructed from sh-KPNA4-2 vector; (4) oe-NC group - transfected with lentivirus constructed from the negative control overexpression vector; (5) oe-KPNA4 group - transfected with lentivirus constructed from oe-KPNA4 vector. After 48 h of transfection, RT-qPCR was performed to examine mRNA levels and validate the efficiency of knockdown and overexpression. The plasmids involved were designed and synthesized by Guangzhou Reebok Biotechnology Co., Ltd.

RT-qPCR for relative expression levels of the Target Gene

Total RNA was extracted from tumor tissue or cells using TRIzol reagent (Invitrogen, USA) according to the manufacturer's instructions. Approximately 1 μg of RNA from each sample was used to synthesize complementary DNA (cDNA) using the Hifair® II 1st Strand cDNA Synthesis SuperMix for qPCR (gDNA digester plus Yeasen Biotech). Total DNA was extracted from cells using the AxyPrep™ Multisource Genomic DNA Miniprep Kit (Axygen, USA). RT-qPCR was performed using the Hieff UNICON® qPCR SYBR Green Master Mix (Yeasen Biotech) on the LightCycler®480 real-time PCR system (Roche Applied Science, Germany). Specific primers for each gene were synthesized by TaKaRa (Table S5), with GAPDH serving as the reference gene. The relative expression levels of each gene were analyzed using the $2^{-\Delta\Delta Ct}$ method, where $\triangle\triangle Ct$ = (average Ct value of target gene in the experimental group - average Ct value of reference gene in the experimental group) - (average Ct value of target gene in the control group - average Ct value of reference gene in the control group) [57]. All RT-qPCR experiments were performed in triplicate.

Western blot of relative expression levels of the target protein

Cell and tissue total protein was extracted using RIPA lysis buffer (Beyotime Biotechnology, Shanghai) and incubated on ice for 30 min. The supernatant was

collected by centrifugation at 8,000 g for 10 min at 4 °C. The protein concentration was quantified using the BCA assay kit (ThermoFisher, USA). After separation by SDS-PAGE, the proteins were transferred onto PVDF membranes (Millipore, Darmstadt, Germany). The membranes were blocked with 5% BSA at room temperature for 1 h, followed by overnight incubation at 4 °C with primary antibodies (Table S6). The membranes were washed three times with TBST for 10 min each and then incubated with HRP-conjugated secondary antibodies, rabbit anti-goat IgG H&L (ab97051, 1:2000, Abcam, UK), and goat anti-mouse (ab205719, 1:2000, Abcam, Cambridge, UK) for 1 h. After TBST washing, the membranes were placed on a clean glass plate. Equal amounts of A and B solutions of the ECL fluorescence detection kit (abs920, Elabscience, Shanghai, China) were mixed and then added to the membranes in a darkroom. The relative protein contents were analyzed using Quantity One V4.6.2 software from BIO-RAD (USA), with the grayscale values of the GAPDH protein bands representing the relative protein levels [58]. The experiment was repeated three times, and the average values were taken.

Cell viability assay

For cell seeding, 5000 cells per well were plated in a 96-well plate and treated with SF (Y0002098, Sigma-Aldrich) at a concentration of 5 µM for 24 h. Subsequently, cell growth inhibition was measured using a real-time cell analysis system (xCELLigence, Agilent) following the manufacturer's instructions, with cell growth data collected automatically every 5 min [59].

In addition, cell viability was assessed using the CCK-8 assay kit (K1018, Apexbio, USA) [60]. In a 96-well plate, 5000 cells per well were seeded for the following two groups: (1) treated with SF at concentrations of 0.2, 4, 6, 8, and 10 µM for 24 h; (2) treated with various concentrations of ICG (cas: 1686147-55-6, Qi Yue Bio) including 0.08, 0.156, 0.313, 0.625, 1.25, 2.5, 5, and 10 µg/mL of ICG, HPG, HPRG, SF+ICG, HPG@SF, and HPRG@SF for 24/48 hours, with or without exposure to a 808 nm laser (MDL-III-808 nm-2000 mW, Changchun New Industry Optoelectronics Technology Co., Ltd.) at an intensity of 200 mW/cm^2 for 30 min. Thereafter, the absorbance value at 450 nm was measured after incubating the cells from each group in the working solution (10 µL CCK-8 assay solution and 100 µL DMEM) for approximately 1 h.

Cellular ROS Detection

HCC cells (1.5×10^5 cells per well) were subjected to the following treatments: (1) addition of PBS under hypoxia; (2) incubation with ICG under hypoxia for 24 h, with/without laser irradiation; (3) incubation with ICG+Hb under hypoxia for 24 h, with/without laser irradiation; (4)

incubation with HPG under hypoxia for 24 h, with/without laser irradiation; (5) incubation with HPRG under hypoxia for 24 h, with/without laser irradiation. The concentration of ICG used was 10 µg/mL, and the concentration of Hb was 200 µg/mL. After each treatment, cells were incubated with 10 µM dichlorodihydrofluorescein (DCFH-DA, C2938, Thermo Fisher) for 4 h. Laser irradiation was performed under the condition of an 808 nm laser at an intensity of 200 mW/cm^2 for 1 min. Cells were washed three times with PBS and stained with DAPI to visualize the cell nucleus. Finally, the fluorescence of DCF was observed using a confocal laser scanning microscope (CLSM, LSM5 LIVE, Carl Zeiss) [61].

HCC cells (5×10^5 cells per well) were subjected to the following treatments: (1) addition of PBS under normoxia and hypoxia, respectively; (2) incubation with 5 µM SF under normoxia and hypoxia for 48 h, respectively; (3) overexpression of KPNA4 under normoxia and silencing of KPNA4 under hypoxia, followed by incubation with 5 µM SF for 48 h; (4) incubation with Hb and 5 µM SF under hypoxia for 48 h; (5) incubation with HPG and 5 µM SF under hypoxia for 48 h; (6) incubation with HPRG and 5 µM SF under hypoxia for 48 h; (7) incubation with ICG under hypoxia for 24 h, with/without laser irradiation; (8) incubation with ICG+Hb under hypoxia for 24 h, with/without laser irradiation; (9) incubation with HPG under hypoxia for 24 h, with/without laser irradiation; (10) incubation with HPRG under hypoxia for 24 h, with/without laser irradiation. The concentration of ICG used was 1 µg/mL, and the concentration of Hb was 20 µg/mL. Laser irradiation was performed under the condition of an 808 nm laser at an intensity of 200 mW/cm^2 for 1 min. After different treatments, HCC cells were harvested and washed with PBS. Subsequently, cells were incubated with 10 µM DCFH-DA at 37 °C in the dark for 1 h. Flow cytometry analysis was carried out using the BD LSRFortessa cell analyzer (BD Biosciences, USA) and analyzed using FlowJo software.

Mitochondrial membrane potential (MMP) detection

Mitochondrial membrane potential was measured using the JC-1 mitochondrial staining kit (40706ES60, Yeasen Biotech). Cells from different groups were incubated with 2 µM JC-1 for 15 min without illumination. Flow cytometry analysis was performed using the BD LSRFortessa cell analyzer [62].

Oxygen consumption rate (OCR) detection

OCR measurements were conducted using the Seahorse XF Pro analyzer (Agilent). Approximately 2×10^4 cells were seeded into each well. After measuring the basal OCR, sequential injections of 1 µM oligomycin (Sigma-Aldrich, USA, Cat. No. 1404-19-9), 0.5 µM FCCP (Sigma-Aldrich, USA, Cat. No. 370-86-5), and 1 µM rotenone/5

μM antimycin A (Sigma-Aldrich, USA, Cat. No. 83-79-4; XY92333, Selleckchem) were performed to determine respiratory capacity [26].

Transmission Electron Microscopy (TEM)
After cell collection, they were fixed overnight at 4℃ in 2.5% glutaraldehyde (G5882, Sigma-Aldrich). Following the initial fixation, cells were washed three times with 0.1 M PBS and then subjected to 1 h of further fixation at 4℃ using permeabilization buffer (S2601, Xinxing Bairui). Subsequently, the samples were dehydrated through an ethanol gradient, embedded in acrylic acid resin, and processed for ultra-thin sectioning and lead-uranium staining. The observation was performed using transmission electron microscopy (JEM-1011; JEOL, Tokyo, Japan) [57].

Redox Ratio Measurement
After cell collection, samples were lysed and divided into two parts. One part was used to measure the NADH/NAD+redox ratio using the NAD+/NADH assay kit with WST-8 (S0175, Beyotime), according to the manufacturer's protocol. The other part was used to measure the GSH/GSSG ratio with the GSH and GSSG assay kit (S0053, Beyotime), following the manufacturer's instructions [63].

Preparation of hb derivatives (Hb-NCs)
To prepare Hb-ICG (HG), indocyanine green (ICG) (1 mmol, I2633l, Sigma-Aldrich), 1-ethyl-(3-dimethylaminopropyl) carbodiimide (EDC) (3 mmol, 39,391, Sigma-Aldrich), and N-hydroxysuccinimide (NHS) (4 mmol, 130,672, Sigma-Aldrich) were dissolved in dimethyl sulfoxide (DMSO) (Sigma-Aldrich). The mixture was then added to Hb dissolved in deionized water (DDW) in a ratio of ICG to Hb molar concentration of 1:2. The reaction mixture was stirred for 12 h and then dialyzed against DDW using a 10 kDa molecular weight cutoff (MWCO) dialysis membrane for 24 h to remove reaction by-products and DMSO. Finally, the dialyzed product was freeze-dried to obtain HG, which was stored at -80 °C for further experiments.

Using the same method, Hb-PEG-ICG (HPG) and Hb-PEG-RGD-ICG (HPRG) were prepared, with the difference being the addition of PEG5000 maleimide (mPEG-MAL, PS1-M-5 K, Puren Bio) and RGD PEG 5000 maleimide (RGD-PEG-MAL, Q-0137736, Qi Yue Bio) at a PEG to Hb molar ratio of 4 to the HG reaction mixture, respectively. Hb-PEG (HP) and Hb-PEG-RGD (HPR) were synthesized using the same method without the addition of ICG solution [64].

Characterization of Hb-NCs
The binding of ICG and PEG was assessed using SDS-PAGE. Hb and its derivatives (Hg, HP, HPG, HPR, and HPRG) were electrophoresed at 120 V for 140 min. The gel was then stained with BaI_2 (566,268, Sigma-Aldrich), with the gel soaked in 5% $BaCl_2$ for 10 min, followed by staining with 0.05 M iodine for 5 min and detection of PEG using deionized water. Subsequently, the same gel was stained with Coomassie Blue to detect the proteins. Hb-NCs were analyzed using MALDI-TOF MS (Voyager DE-STR; Applied Biosystems Inc., Foster, California, USA). The Zeta potential of Hb-NCs was evaluated using a Zetasizer Ultra (Malvern Instruments Ltd., Malvern, UK). UV-Vis spectrophotometry (Thermo Fisher Scientific) was used to obtain absorbance curves of ICG and Hb-NCs in the wavelength range of 400–920 nm, and the ICG content was calculated [64].

Dissolved oxygen (DO) measurement
Phosphate buffered saline (PBS; 25 mL) was purged with nitrogen for 10 min and then sealed to remove oxygen. The PBS, ICG, Hb, HG, HPG, and HPRG (5 mg Hb/mL) were bubbled for 1 min using an oxygen bubbling method and injected into the deoxygenated PBS using a syringe. The DO level was monitored using a DO meter (YK-2001-PHA; Lutron, Coopersburg, PA, USA) [64].

Generation of Singlet Oxygen
The production of singlet oxygen by Hb-NCs was quantified using the SOSG reagent (S36002, Thermo Fisher Scientific). ICG, HG, HPG, and HPRG were mixed with the SOSG solution, resulting in a final ICG concentration of 1 μg/mL. The samples were exposed to laser irradiation (808 nm) with an intensity of 10.5 mW/cm². The fluorescence intensity of the peroxides within SOSG was measured at 0, 10, 20, 30, 40, and 60 min of laser irradiation using a microplate reader (Infinite 200; Tecan Inc., Mannedorf, Switzerland) with excitation and emission wavelengths of 510 nm and 560 nm, respectively. As a negative control, Hb, HP, and HPR were also tested using the same protocol [65].

Preparation and characterization of SF-loaded Hb-NCs
SF-loaded Hb-NCs were prepared using a small amount of organic solvent. Firstly, 3 mg of SF was dissolved in DMSO, while 5 mg of Hb or Hb-NCs was dissolved in DDW, followed by ball milling for 5 min. The mixture was then diluted tenfold and freeze-dried, and subsequently re-dissolved in DDW and filtered through a 0.5 μm syringe filter to obtain SF-loaded Hb-NCs (SF@Hb, SF@HG, HPG@SF, HPRG@SF). The average diameter and zeta potential of the NCs were evaluated using a Zetasizer Ultra. The samples were placed on 200-mesh carbon-coated copper grids, negatively stained with

Wang *et al. Journal of Nanobiotechnology*   (2024) 22:473

Page 21 of 25

uranyl acetate, and observed for morphology using TEM [64].

Colloidal Stability and in Vitro Release of SF

We simulated the colloidal stability of Hb-NCs loaded with SF under physiological conditions. Hb-NCs were dispersed in FBS or PBS at pH 5.5, 6.8, and 7.4 and then incubated in an oscillating water bath (50 rpm; 37℃). The average diameter of the NCs was monitored at 0, 1, 4, 8, and 12 h using a Zetasizer Ultra (Malvern Instruments Ltd.).

The release of SF was evaluated using dialysis. A 150 μL suspension of Hb-NCs was loaded into a DiaEasy dialysis tube (MWCO: 6–8 kDa; AmyJet Scientific) and immersed in a release medium (2 mL of PBS at pH 5.5, 6.8, and 7.4). After incubating for 2, 4, 8, 12, 24, 48, 72, 96, and 120 h in an oscillating water bath (50 rpm; 37℃), the tubes containing the loaded NCs were transferred to new containers and filled with fresh release medium (2 mL). The release amount of SF in PBS was determined using a high-performance liquid chromatography (HPLC) system (Agilent 1260 Infinity; Agilent Technologies, Palo Alto, CA, USA) equipped with a phenomenex C8 chromatography column (250 mm × 4.6 μm × 5 μm). The mobile phase consisted of a triethylamine-phosphoric acid buffer-acetonitrile mixture (60:40). Detection was performed at a wavelength of 265 nm, with a flow rate of 1.0 mL/min, a column temperature of 35℃, and an injection volume of 20 μL [66].

HCC cell uptake in monolayer culture model

A total of 1×10^3 hypoxic MHCC97H cells were seeded in a 96-well plate. The MHCC97H cells were co-incubated with ICG, HPG@SF, HPRG@SF, and HPRG@SF+free RGD for 4 h, while HPRG@SF and 3 mM RGD were simultaneously treated with the cells for 1 h. The concentrations of SF and ICG used were both 50 μg/mL. PBS was used as a control. The cells were fixed with a 4% (v/v) formaldehyde solution and stained with DAPI. The fluorescence signals of ICG and DAPI were observed using CLSM. Additionally, the fluorescence intensity of ICG in each group of MHCC97H cells was quantitatively detected using a flow cytometer [67].

Cellular Uptake in HCC Spheroid Culture Model

Cellular uptake studies were conducted in a hypoxic MHCC97H spheroid model. MHCC97H cells were seeded on a round-bottom 96-well plate pre-coated with agarose gel and cultured under the same conditions as the monolayer model. After 7 days of culture, the spheroids were treated with ICG solution, HPG@SF, and HPRG@SF+free RGD (with SF concentration at 50 μg/mL, ICG concentration at 50 μg/mL, and free RGD concentration at 2 μM) and incubated for 24 h. The spheroids were then

washed with PBS three times and fixed with a 4% (v/v) formaldehyde solution. The fluorescence signal of ICG was observed using the Z-stack function [64].

In Vitro Hypoxia Relief Experiment

MHCC97H cells were seeded into a 6-well plate at a density of 5.0×10^5 cells per well and cultured at 37 °C for 24 h. After culturing the cells in the presence of Hb, HPG, HPRG, HPG@SF, or HPRG@SF (SF concentration: 50 μg/mL; Hb concentration: 200 μg/mL) for 4 h, Hypoxia Green reagent (H20035, Thermo Fisher Scientific) was added and incubated for 2 h. The fluorescence intensity of the reagent was measured using flow cytometry (FACS Canto™ II; BD Biosciences).

Immunofluorescence staining of HIF-1α was performed on hypoxic MHCC97H cells. The cells were co-incubated with Hb, HPG, HPRG, HPG@SF, or HPRG@SF (SF concentration: 50 μg/mL; Hb concentration: 200 μg/mL) for 4 h, then fixed with methanol for 5 min and incubated overnight at 4 °C with Alexa Fluor® 488 anti-HIF-1α antibody (ab190197; Abcam, Cambridge, MA, USA). After nuclear staining with DAPI, the samples were observed using confocal laser scanning microscopy [64].

In Vitro cytotoxicity testing based on HCC Cell spheroids

The hypoxic MHCC97H cells were cultured in 3D cell culture dishes (LabToLab, Daejeon, Korea) at a density of 2.5×10^6 cells per dish, and MHCC97H spheroids formed spontaneously within 24 h. On the 2nd and 4th days, the cells were treated with free SF, free ICG, SF+ICG, HPG@SF, or HPRG@SF (corresponding to 2 μg/mL SF and 2 μg/mL ICG) and incubated for 24 h. On the 3rd and 5th days, the cells were irradiated with an 808 nm laser (200 mW/cm²) for 1 h. The morphology of MHCC97H spheroids was observed using an Axiovert 25 microscope (Carl Zeiss) on the 1st and 7th days. The volume (V, mm³) of the spheroids was calculated by the formula: V=0.5× longest diameter× (shortest diameter)²/2 [64].

Subcutaneous transplant Tumor Model of HCC in Nude mice

A total of 34 BALB/c nude mice (strain: 211) were purchased from Beijing Weitonglihua Experimental Technology Co., Ltd. The mice were approximately 4 weeks old and weighed around 15 g. They were individually housed in cages in an SPF-grade animal laboratory, with a humidity of 60–65% and a temperature of 22–25℃. The mice were maintained on a 12-hour light/dark cycle and had ad libitum access to food and water. After one week of acclimation to the housing conditions, the health of the nude mice was observed before starting the experiments. All animal experiments were performed in accordance

with the guidelines outlined in our institution's "Guidelines for the Care and Use of Laboratory Animals."

A total of 6.0×10^6 anaerobically cultured MHCC97H cells were subcutaneously injected into the right upper lumbar region of the nude mice. The tumor volume (V, mm^3) was calculated using the following formula: V=0.5×longest diameter×(shortest diameter)^2/2, as described in a previous study [68]. Subsequent experiments were conducted accordingly.

Biodistribution of HPRG@SF
When the average tumor volume in the xenograft nude mice reached approximately 100 mm^3, SF+ICG, HPG@SF, or HPRG@SF was intravenously injected at a dose of 50 μg/kg through the tail vein. At 2, 4, 6, 8, and 24 h post-injection, whole-body fluorescence imaging was performed using a near-infrared imaging system for small animals. After 24 h post-injection, the liver, spleen, kidneys, heart, lungs, and tumor were dissected, and the fluorescence intensity of each organ or tissue was measured.

Intratumoral imaging of tumor tissue: After collecting the tumor tissue, it was subjected to ex vivo fluorescence imaging, fixed in 4% paraformaldehyde for 24 h, and then placed in a 15% sucrose-PBS solution for 24 h until settlement occurred. Subsequently, the tumor tissue was placed in 30% sucrose for 24 h until settlement. The tumor tissue was then prepared into frozen sections with a thickness of 20 mm and stained with 1 mg/mL DAPI for 10 min at room temperature. After twice washing with PBS (pH 7.4), the sections were immediately examined under a CLSM [69, 70]. There were three animals per group.

Targeted Therapy-PDT Combined Therapy in HCC Subcutaneous Transplant Tumor Nude Mouse Model
After the tumor volume reached approximately 30–50 mm^3, nude mice were randomly divided into five groups: PBS group, SF solution group (SF), SF and ICG solution group (SF+ICG), HPG@SF group, and HPRG@SF group. Tumor size and body weight were monitored daily for 15 days. The drugs were administered via tail vein injection on days 1, 3, 5, 7, 9, 11, and 13, with a dosage of 5 mg/kg for both SF and ICG. Six hours after the first injection, the SF+ICG group, HPG@SF group, and HPRG@SF group were subjected to 808 nm laser treatment (power density of 300 mW/cm^2 for 5 min), which continued until day 15. The body weight and tumor volume of the nude mice were monitored during the treatment period, and the tumor volume calculation was conducted using the formula V=0.5 × the longest diameter × (the shortest diameter)^2/2 [64]. Each group consisted of five nude mice.

Biocompatibility of HPRG@SF
On the 15th day, we dissected the tumors and conducted weighing under isoflurane anesthesia. A blood sample of 0.5 mL was collected from the left ventricle, and a complete blood cell count (CBC) test was performed using Scil Vet abc Plus (Scil Animal Care). Serum samples were obtained by centrifuging the blood samples at 13,000×g for 5 min. Fuji Dri-Chem 3500 s (Fujifilm Holdings Co., Ltd., Tokyo, Japan) was utilized to analyze the levels of serum albumin (ALB), aspartate aminotransferase (AST), alanine aminotransferase (ALT), serum creatinine (SCr), and blood urea nitrogen (BUN).

Subsequently, we euthanized the nude mice using CO_2 and then dissected the tumors and major organs for weighing. H&E staining was performed on the major organs: the tissues were initially rinsed with saline solution and fixed in 4% paraformaldehyde for 30–50 min, followed by water washes, dehydration, transparency, embedding in paraffin, and sectioning. The tissue sections were flattened and attached to glass slides, dried in a constant temperature incubator at 45℃, and then dewaxed with xylene, followed by a 2-minute wash with decreasing concentrations of ethanol and distilled water. Subsequently, the sections were stained with hematoxylin for 5 min, rinsed off excess stain under tap water, differentiated in 1% hydrochloric acid ethanol for 3 s, stained with 5% eosin solution for approximately 2 min, followed by dehydration, clearing, and mounting. Finally, the tissue sections were observed under a microscope [71].

Statistical analysis
All experimental data were processed using GraphPad Prism 8.0. Non-paired t-tests were conducted to compare the data between two groups, while a one-way analysis of variance (ANOVA) was employed to compare data among multiple groups. The homogeneity of variance was assessed using Levene's test. If the variance was homogeneous, Dunnett's t test and LSD-t test were applied for pairwise comparisons. If the variance was not homogeneous, Dunnett's T3 test was used. A significance level of $P<0.05$ indicated a statistically significant difference between the two groups' data.

Abbreviations
HCC	Hepatocellular carcinoma
ICG	Indocyanine green
PDT	Photodynamic therapy
CNVs	Copy number variations

Supplementary Information
The online version contains supplementary material available at https://doi.org/10.1186/s12951-024-02717-9.

> Supplementary Material 1
>
> Supplementary Material 2

Supplementary Material 3

Supplementary Material 4

Supplementary Material 5

Supplementary Material 6

Supplementary Material 7

Supplementary Material 8

Supplementary Material 9

Supplementary Material 10

Supplementary Material 11

Supplementary Material 12

Supplementary Material 13

Supplementary Material 14

Supplementary Material 15

Author contributions
Yiliang Wang: Conceptualization; Formal analysis; Methodology; Visualization; Writing - original draft; Writing - review & editing. Nu Li: Conceptualization; Formal analysis; Methodology; Visualization; Writing - original draft; Writing - review & editing. Letian Qu: Conceptualization; Formal analysis; Methodology; Visualization; Writing - original draft; Writing - review & editing. Mu Zhang: Data curation; Formal analysis; Investigation. Zhuo Li: Data curation; Investigation; Validation; Writing - review & editing. Dasheng Cai: Conceptualization; Funding acquisition; Resources; Project administration; Supervision; Writing - review & editing. Xiang Li: Conceptualization; Resources; Project administration; Supervision; Writing - review & editing.

Data availability
The data underlying this article will be shared on reasonable request to the corresponding author.

Declarations

Ethical statement
All experiments involving mice were approved by the Animal Ethics Committee of The First Hospital of China Medical University and conducted in strict accordance to the standard of the Guide for the Care and Use of Laboratory Animals published by the Ministry of Science and Technology of the People's Republic of China in 2006.

Consent for publication
Not applicable.

Competing interests
The authors declare no competing interests.

References
1. Gallage S, Avila JEB, Ramadori P, et al. A researcher's guide to preclinical mouse NASH models. Nat Metab. 2022;4(12):1632–49. https://doi.org/10.1038/s42255-022-00700-y.
2. Sas Z, Cendrowicz E, Weinhäuser I, Rygiel TP. Tumor Microenvironment of Hepatocellular Carcinoma: challenges and opportunities for New Treatment options. Int J Mol Sci. 2022;23(7):3778. https://doi.org/10.3390/ijms23073778. Published 2022 Mar 29.
3. Zou S, Chen S, Rao G, et al. Extrachromosomal circular MiR-17-92 amplicon promotes HCC. Hepatology. 2024;79(1):79–95. https://doi.org/10.1097/HEP.0000000000000435.
4. Zhou YW, Li QF, Chen YY, et al. Clinicopathologic features, treatment, survival, and prognostic factors of combined hepatocellular and cholangiocarcinoma: a nomogram development based on SEER database and validation in multi-center study. Eur J Surg Oncol. 2022;48(7):1559–66. https://doi.org/10.1016/j.ejso.2022.01.023.
5. Toyota A, Goto M, Miyamoto M, et al. Novel protein kinase cAMP-Activated Catalytic Subunit Alpha (PRKACA) inhibitor shows anti-tumor activity in a fibrolamellar hepatocellular carcinoma model. Biochem Biophys Res Commun. 2022;621:157–61. https://doi.org/10.1016/j.bbrc.2022.07.008.
6. Zhong T, Zhang W, Guo H, et al. The regulatory and modulatory roles of TRP family channels in malignant tumors and relevant therapeutic strategies. Acta Pharm Sin B. 2022;12(4):1761–80. https://doi.org/10.1016/j.apsb.2021.11.001.
7. You Y, Wen D, Zeng L, et al. ALKBH5/MAP3K8 axis regulates PD-L1 + macrophage infiltration and promotes hepatocellular carcinoma progression. Int J Biol Sci. 2022;18(13):5001–18. https://doi.org/10.7150/ijbs.70149. Published 2022 Aug 1.
8. Li K, Gong Y, Qiu D, et al. Hyperbaric oxygen facilitates teniposide-induced cGAS-STING activation to enhance the antitumor efficacy of PD-1 antibody in HCC. J Immunother Cancer. 2022;10(8):e004006. https://doi.org/10.1136/jitc-2021-004006.
9. Vaupel P, Schmidberger H, Mayer A. The Warburg effect: essential part of metabolic reprogramming and central contributor to cancer progression. Int J Radiat Biol. 2019;95(7):912–9. https://doi.org/10.1080/09553002.2019.1589653.
10. Zhang LY, Zhang JG, Yang X, Cai MH, Zhang CW, Hu ZM. Targeting Tumor Immunosuppressive Microenvironment for the Prevention of hepatic Cancer: applications of Traditional Chinese Medicines in targeted delivery. Curr Top Med Chem. 2020;20(30):2789–800. https://doi.org/10.2174/1568026620666201019111524.
11. Wu Q, Zhou W, Yin S, et al. Blocking triggering receptor expressed on myeloid cells-1-Positive Tumor-Associated macrophages Induced by Hypoxia reverses immunosuppression and anti-programmed cell death Ligand 1 resistance in Liver Cancer. Hepatology. 2019;70(1):198–214. https://doi.org/10.1002/hep.30593.
12. Chen X, Li C, Liu H. Enhanced recombinant protein production under Special Environmental stress. Front Microbiol. 2021;12:630814. https://doi.org/10.3389/fmicb.2021.630814. Published 2021 Apr 15.
13. Lan Q, Cao Z, Yang X, Gu Z. Physiological and Proteomic Responses of Dairy Buffalo to Heat Stress Induced by Different Altitudes. Metabolites. 2022;12(10):909. Published 2022 Sep 27. https://doi.org/10.3390/metabo12100909.
14. Shi Z, Li Z, Jin B, et al. Loss of LncRNA DUXAP8 synergistically enhanced sorafenib induced ferroptosis in hepatocellular carcinoma via SLC7A11 de-palmitoylation. Clin Transl Med. 2023;13(6):e1300. https://doi.org/10.1002/ctm2.1300.
15. Su TH, Wu CH, Liu TH, Ho CM, Liu CJ. Clinical practice guidelines and real-life practice in hepatocellular carcinoma: a Taiwan perspective. Clin Mol Hepatol. 2023;29(2):230–41. https://doi.org/10.3350/cmh.2022.0421.
16. Xiao Y, Xu Z, Cheng Y et al. Fe^{3+}-binding transferrin nanovesicles encapsulating sorafenib induce ferroptosis in hepatocellular carcinoma. Biomater Res. 2023;27(1):63. Published 2023 Jul 1. https://doi.org/10.1186/s40824-023-00401-x.
17. Li Z, Caron de Fromentel C, Kim W, et al. RNA helicase DDX5 modulates sorafenib sensitivity in hepatocellular carcinoma via the Wnt/β-catenin-ferroptosis axis. Cell Death Dis. 2023;14(11):786. https://doi.org/10.1038/s41419-023-06302-0. Published 2023 Nov 30.
18. Jiang B, Zhang H, Wu Y, Shen Y. Single-cell immune ecosystem and metabolism reprogramming imprinted by psoriasis niche. Ann Transl Med. 2022;10(15):837. https://doi.org/10.21037/atm-22-1810.
19. Liu H, Prashant NM, Spurr LF, et al. scReQTL: an approach to correlate SNVs to gene expression from individual scRNA-seq datasets. BMC Genomics. 2021;22(1):40. https://doi.org/10.1186/s12864-020-07334-y. Published 2021 Jan 8.
20. Cun X, Jansman MMT, Liu X, Boureau V, Thulstrup PW, Hosta-Rigau L. Hemoglobin-stabilized gold nanoclusters displaying oxygen transport ability, self-antioxidation, auto-fluorescence properties and long-term

storage potential. RSC Adv. 2023;13(23):15540–53. https://doi.org/10.1039/d3ra00689a. Published 2023 May 23.

21. Ma X, Yang S, Zhang T, et al. Bioresponsive immune-booster-based prodrug nanogel for cancer immunotherapy. Acta Pharm Sin B. 2022;12(1):451–66. https://doi.org/10.1016/j.apsb.2021.05.016.

22. Gao J, Qin H, Wang F, et al. Hyperthermia-triggered biomimetic bubble nanomachines. Nat Commun. 2023;14(1):4867. https://doi.org/10.1038/s41467-023-40474-9. Published 2023 Aug 11.

23. Oh A, Kajita H, Matoba E, et al. Photoacoustic lymphangiography before and after lymphaticovenular anastomosis. Arch Plast Surg. 2021;48(3):323–8. https://doi.org/10.5999/aps.2020.02404.

24. Xia S, Ji L, Tao L, et al. TAK1 is a Novel Target in Hepatocellular Carcinoma and contributes to Sorafenib Resistance. Cell Mol Gastroenterol Hepatol. 2021;12(3):1121–43. https://doi.org/10.1016/j.jcmgh.2021.04.016.

25. Xia S, Pan Y, Liang Y, Xu J, Cai X. The microenvironmental and metabolic aspects of sorafenib resistance in hepatocellular carcinoma. EBioMedicine. 2020;51:102610. https://doi.org/10.1016/j.ebiom.2019.102610.

26. Smith MD, Robinson SL, Molomjamts M, Wackett LP. In Vivo Assay Reveals Microbial OleA Thiolases Initiating Hydrocarbon and β-Lactone Biosynthesis. mBio. 2020;11(2):e00111-20. Published 2020 Mar 10. https://doi.org/10.1128/mBio.00111-20.

27. Liu X, Zhang Y, Lu W, et al. Mitochondrial TXNRD3 confers drug resistance via redox-mediated mechanism and is a potential therapeutic target in vivo. Redox Biol. 2020;36:101652. https://doi.org/10.1016/j.redox.2020.101652.

28. Taguchi K, Yamasaki K, Maruyama T, Otagiri M. Comparison of the Pharmaco-kinetic properties of Hemoglobin-based Oxygen Carriers. J Funct Biomater. 2017;8(1):11. https://doi.org/10.3390/jfb8010011. Published 2017 Mar 18.

29. Sheng Z, Hu D, Zheng M, et al. Smart human serum albumin-indocyanine green nanoparticles generated by programmed assembly for dual-modal imaging-guided cancer synergistic phototherapy. ACS Nano. 2014;8(12):12310–22. https://doi.org/10.1021/nn5062386.

30. Sun F, Wang J, Sun Q, et al. Interleukin-8 promotes integrin β3 upregulation and cell invasion through PI3K/Akt pathway in hepatocellular carcinoma. J Exp Clin Cancer Res. 2019;38(1):449. https://doi.org/10.1186/s13046-019-1455-x. Published 2019 Nov 4.

31. Li Y, Hu P, Wang X, Hou X, Liu F, Jiang X. Integrin $\alpha^v\beta^3$-targeted polydopamine-coated gold nanostars for photothermal ablation therapy of hepatocellular carcinoma. Regen Biomater. 2021;8(5):rbab046. https://doi.org/10.1093/rb/rbab046. Published 2021 Aug 10.

32. Khan MA, Ali S, Venkatraman SS, Sohail MF, Ovais M, Raza A. Fabrication of poly (butadiene-block-ethylene oxide) based amphiphilic polymersomes: an approach for improved oral pharmacokinetics of Sorafenib. Int J Pharm. 2018;542(1–2):196–204. https://doi.org/10.1016/j.ijpharm.2018.03.023.

33. Kong FH, Ye QF, Miao XY, et al. Current status of sorafenib nanoparticle delivery systems in the treatment of hepatocellular carcinoma. Theranostics. 2021;11(11):5464–90. https://doi.org/10.7150/thno.54822. Published 2021 Mar 13.

34. Liu S, Liu Y, Chang Q, Celia C, Deng X, Xie Y. pH-Responsive Sorafenib/Iron-Co-Loaded Mesoporous Polydopamine nanoparticles for synergistic ferroptosis and Photothermal Therapy. Biomacromolecules. 2024;25(1):522–31. https://doi.org/10.1021/acs.biomac.3c01173.

35. Yin S, Jin W, Qiu Y, Fu L, Wang T, Yu H. Solamargine induces hepatocellular carcinoma cell apoptosis and autophagy via inhibiting LIF/miR-192-5p/CYR61/Akt signaling pathways and eliciting immunostimulatory tumor microenvi-ronment. J Hematol Oncol. 2022;15(1):32. Published 2022 Mar 21. https://doi.org/10.1186/s13045-022-01248-w.

36. Chen J, Li H, Zhang B, et al. ABI2-mediated MEOX2/KLF4-NANOG axis promotes liver cancer stem cell and drives tumour recurrence. Liver Int. 2022;42(11):2562–76. https://doi.org/10.1111/liv.15412.

37. Chen C, Lin HG, Yao Z, et al. Transcription factor glucocorticoid modulatory element-binding protein 1 promotes hepatocellular carcinoma progres-sion by activating yes-associate protein 1. World J Gastrointest Oncol. 2023;15(6):988–1004. https://doi.org/10.4251/wjgo.v15.i6.988.

38. Choi SH, Park JY. Regulation of the hypoxic tumor environment in hepatocel-lular carcinoma using RNA interference [published correction appears in Can-cer Cell Int. 2017;17:69. https://doi.org/10.1186/s12935-017-0438-2]. Cancer Cell Int. 2017;17:3. Published 2017 Jan 3. doi:10.1186/s12935-016-0374-6.

39. Liang Y, Zhang R, Biswas S, et al. Integrated single-cell transcriptomics reveals the hypoxia-induced inflammation-cancer transformation in NASH-derived hepatocellular carcinoma. Cell Prolif. 2024;57(4):e13576. https://doi.org/10.1111/cpr.13576.

40. Zhang Z, Wang X. Roles of long non-coding RNAs in digestive tract cancer and their clinical application. Zhejiang Da Xue Xue Bao Yi Xue Ban. 2023;52(4):451–9. https://doi.org/10.3724/zdxbyxb-2023-0169.

41. Egners A, Rezaei M, Kuzmanov A, et al. PHD3 acts as Tumor suppressor in mouse Osteosarcoma and influences Tumor Vascularization via PDGF-C signaling. Cancers (Basel). 2018;10(12):496. https://doi.org/10.3390/can-cers10120496. Published 2018 Dec 6.

42. Li L, Zou W, Xiao Z, Deng Z, Liu R. Hypoxia-induced long non-coding RNA LSAMP-AS1 regulates ceRNA Network to Predict Prognosis for Pancreatic Cancer. Comb Chem High Throughput Screen. 2023;26(13):2358–71. https://doi.org/10.2174/1386207326666230314112238.

43. Tseeleesuren D, Hsiao HH, Kant R et al. The Expression and Prognostic Value of Cancer Stem Cell Markers, NRF2, and Its Target Genes in TAE/TACE-Treated Hepatocellular Carcinoma. Medicina (Kaunas). 2022;58(2):212. Published 2022 Feb 1. https://doi.org/10.3390/medicina58020212.

44. Qian Y, Li Y, Zheng C, et al. High methylation levels of histone H3 lysine 9 associated with activation of hypoxia-inducible factor 1α (HIF-1α) predict patients' worse prognosis in human hepatocellular carcinomas. Cancer Genet. 2020;245:17–26. https://doi.org/10.1016/j.cancergen.2020.04.077.

45. Liu XW, Cai TY, Zhu H, et al. Q6, a novel hypoxia-targeted drug, regulates hypoxia-inducible factor signaling via an autophagy-dependent mechanism in hepatocellular carcinoma. Autophagy. 2014;10(1):111–22. https://doi.org/10.4161/auto.26838.

46. Zhang LF, Lou JT, Lu MH, et al. Suppression of miR-199a maturation by HuR is crucial for hypoxia-induced glycolytic switch in hepatocellular carcinoma. EMBO J. 2015;34(21):2671–85. https://doi.org/10.15252/embj.201591803.

47. Zhu GQ, Tang Z, Huang R, et al. CD36⁺ cancer-associated fibroblasts provide immunosuppressive microenvironment for hepatocellular carcinoma via secretion of macrophage migration inhibitory factor. Cell Discov. 2023;9(1):25. https://doi.org/10.1038/s41421-023-00529-z. Published 2023 Mar 6.

48. Yao RQ, Li ZX, Wang LX, et al. Single-cell transcriptome profiling of the immune space-time landscape reveals dendritic cell regulatory program in polymicrobial sepsis. Theranostics. 2022;12(10):4606–28. https://doi.org/10.7150/thno.72760. Published 2022 May 29.

49. Wang Y, Fan JL, Melms JC, et al. Multimodal single-cell and whole-genome sequencing of small, frozen clinical specimens. Nat Genet. 2023;55(1):19–25. https://doi.org/10.1038/s41588-022-01268-9.

50. Tan Z, Chen X, Zuo J, Fu S, Wang H, Wang J. Comprehensive analysis of scRNA-Seq and bulk RNA-Seq reveals dynamic changes in the tumor immune microenvironment of bladder cancer and establishes a prognostic model. J Transl Med. 2023;21(1):223. https://doi.org/10.1186/s12967-023-04056-z. Published 2023 Mar 27.

51. Huang M, Yang S, Tai WCS, et al. Bioinformatics Identification of Regulatory Genes and mechanism related to Hypoxia-Induced PD-L1 inhibitor resistance in Hepatocellular Carcinoma. Int J Mol Sci. 2023;24(10):8720. https://doi.org/10.3390/ijms24108720. Published 2023 May 13.

52. Shi M, Dai WQ, Jia RR, et al. APC^{CDC20}-mediated degradation of PHD3 stabi-lizes HIF-1a and promotes tumorigenesis in hepatocellular carcinoma. Cancer Lett. 2021;496:144–55. https://doi.org/10.1016/j.canlet.2020.10.011.

53. Lu J, Yu C, Bao Q, Zhang X, Wang J. Identification and analysis of necroptosis-associated signatures for prognostic and immune microenvironment evalua-tion in hepatocellular carcinoma. Front Immunol. 2022;13:973649. https://doi.org/10.3389/fimmu.2022.973649. Published 2022 Aug 23.

54. Wu G, Zheng K, Xia S, et al. MicroRNA-655-3p functions as a tumor suppressor by regulating ADAM10 and β-catenin pathway in Hepatocellular Carcinoma. J Exp Clin Cancer Res. 2016;35(1):89. https://doi.org/10.1186/s13046-016-0368-1. Published 2016 Jun 4.

55. Liang C, Dong Z, Cai X, et al. Hypoxia induces sorafenib resistance mediated by autophagy via activating FOXO3a in hepatocellular carcinoma. Cell Death Dis. 2020;11(11):1017. https://doi.org/10.1038/s41419-020-03233-y. Published 2020 Nov 29.

56. Haga K, Fujimoto A, Takai-Todaka R, et al. Functional receptor molecules CD300lf and CD300ld within the CD300 family enable murine noroviruses to infect cells. Proc Natl Acad Sci U S A. 2016;113(41):E6248–55. https://doi.org/10.1073/pnas.1605575113.

57. Xu J, Ji L, Ruan Y et al. UBQLN1 mediates sorafenib resistance through regu-lating mitochondrial biogenesis and ROS homeostasis by targeting PGC1β in hepatocellular carcinoma. Signal Transduct Target Ther. 2021;6(1):190. Published 2021 May 18. https://doi.org/10.1038/s41392-021-00594-4.

58. Liu H, Xue Q, Cai H et al. RUNX3-mediated circDYRK1A inhibits glutamine metabolism in gastric cancer by up-regulating microRNA-889-3p-dependent

FBXO4. J Transl Med. 2022;20(1):120. Published 2022 Mar 10. https://doi.org/10.1186/s12967-022-03286-x.

59. Chen CY, Chen CC, Shieh TM et al. Corylin Suppresses Hepatocellular Carcinoma Progression via the Inhibition of Epithelial-Mesenchymal Transition, Mediated by Long Noncoding RNA GAS5. Int J Mol Sci. 2018;19(2):380. Published 2018 Jan 27. https://doi.org/10.3390/ijms19020380.

60. Hu Y, Wen Q, Cai Y, et al. Alantolactone induces concurrent apoptosis and GSDME-dependent pyroptosis of anaplastic thyroid cancer through ROS mitochondria-dependent caspase pathway. Phytomedicine. 2023;108:154528. https://doi.org/10.1016/j.phymed.2022.154528.

61. Kim JK, Jang HD. Nrf2-mediated HO-1 induction coupled with the ERK signaling pathway contributes to indirect antioxidant capacity of caffeic acid phenethyl ester in HepG2 cells. Int J Mol Sci. 2014;15(7):12149–65. https://doi.org/10.3390/ijms150712149. Published 2014 Jul 9.

62. Dong H, Feng Y, Yang Y, et al. A novel function of mitochondrial phosphoenolpyruvate carboxykinase as a Regulator of Inflammatory Response in Kupffer cells. Front Cell Dev Biol. 2021;9:726931. https://doi.org/10.3389/fcell.2021.726931. Published 2021 Dec 14.

63. Liu H, Qiao J, Shangguan J, Zhu J. Effects of glutamate oxaloacetate transaminase on reactive oxygen species in Ganoderma Lucidum. Appl Microbiol Biotechnol. 2023;107(5–6):1845–61. https://doi.org/10.1007/s00253-023-12417-3.

64. Lee HS, Yoo SY, Lee SM, et al. Hypoxia-alleviating hemoglobin nanoclusters for sensitizing chemo-photodynamic therapy of cervical cance. Chem Eng J. 2023;457:141224. https://doi.org/10.1016/j.cej.2022.141224.

65. Kim H, Kim Y, Kim IH, Kim K, Choi Y. ROS-responsive activatable photosensitizing agent for imaging and photodynamic therapy of activated macrophages. Theranostics. 2013;4(1):1–11. https://doi.org/10.7150/thno.7101. Published 2013 Dec 1.

66. Peng Y, Yu W, Li E, et al. Discovery of an orally active and liver-targeted Prodrug of 5-Fluoro-2′-Deoxyuridine for the Treatment of Hepatocellular Carcinoma. J Med Chem. 2016;59(8):3661–70. https://doi.org/10.1021/acs.jmedchem.5b01807.

67. Wang Y, Wang N, Du Y, et al. Novel nanoparticles prepared from isothiocyanate derivatives for phototherapy of tumor. J Photochem Photobiol B. 2023;242:112701. https://doi.org/10.1016/j.jphotobiol.2023.112701.

68. Jiang R, Xia Y, Li J, et al. High expression levels of IKKalpha and IKKbeta are necessary for the malignant properties of liver cancer. Int J Cancer. 2010;126(5):1263–74. https://doi.org/10.1002/ijc.24854.

69. Lai J, Deng G, Sun Z, et al. Scaffolds biomimicking macrophages for a glioblastoma NIR-Ib imaging guided photothermal therapeutic strategy by crossing blood-brain barrier. Biomaterials. 2019;211:48–56. https://doi.org/10.1016/j.biomaterials.2019.04.026.

70. Xin H, Sha X, Jiang X, Zhang W, Chen L, Fang X. Anti-glioblastoma efficacy and safety of paclitaxel-loading angiopep-conjugated dual targeting PEG-PCL nanoparticles. Biomaterials. 2012;33(32):8167–76. https://doi.org/10.1016/j.biomaterials.2012.07.046.

71. Li H, Wang J, Liu H, et al. Existence of intratumoral tertiary lymphoid structures is associated with immune cells infiltration and predicts better prognosis in early-stage hepatocellular carcinoma. Aging. 2020;12(4):3451–72. https://doi.org/10.18632/aging.102821.

Publisher's Note